2-26-2016

Synthesis of Crystalline, Mesoporous Metal Oxide Catalysts for Environmental and Energy Applications

Zhu Luo
luozhu711@hotmail.com

Synthesis of Crystalline, Mesoporous Metal Oxide Catalysts for Environmental and Energy Applications

Zhu Luo, Ph.D

University of Connecticut, 2016

The main goal of this dissertation study is to develop high activity heterogeneous catalysts (metal oxide materials) for environmental and sustainable energy applications. Controlled synthesis of crystalline structures, physical, and chemical properties of the catalysts result in improved catalytic activity. Four different topics including photocatalytic remediation, hydrogen evolution, electrochemical supercapacitors, and organic synthesis applications are discussed in this thesis.

The first part presents a unique inverse micelle preparation method to synthesize mesoporous mixed phase (anatase/rutile) titanium dioxide materials. This study was conducted with the purpose of developing an inexpensive, environmentally friendly, and visible light active photocatalyst. The prepared vanadium doped mesoporous TiO_2 materials show enhanced photocatalytic activity for decomposing organic pollutants compared to commercial TiO_2 (Degussa P25).

The second part exhibits the preparation of copper modified titanium dioxides materials for terminal alkyne homocoupling reactions. The mesoporous TiO_2 was used as a support. The focus of this study is to investigate how the different preparation methods (doping, solvent free, and impregnation) and the various forms of copper affect the homocoupling yields. The Cu doped TiO_2 material shows the best homocoupling activity

with high yield more than 99%.

In the third part of this thesis, mesoporous MoO_{3-x} materials was prepared via a novel method. The prepared MoO_{3-x} material has a crystalline, mesoporous, and oxygen-deficient structure. The unique physical and chemical properties of MoO_{3-x} make it a potential replacement for Pt materials in hydrogen evolution reactions. The MoO_{3-x} material can be used in both alkaline and acidic media without the assistance of any noble metal catalysts. Further optimization of this study may lead to the low-cost metal oxide catalysts in practical electrochemical applications.

Synthesis of Crystalline, Mesoporous Metal Oxide Catalysts for Environmental and Energy Applications

Zhu Luo

B.S., Central South University of Forestry and Technology, China, 2010

A Dissertation

Submitted in Partial Fulfillment of the

Requirements for the Degree of

Doctor of Philosophy

at the

University of Connecticut

2016

APPROVAL PAGE

Doctor of Philosophy Dissertation

Synthesis of Crystalline, Mesoporous Metal Oxide Catalysts for Environmental and Energy Applications

Presented by

Zhu Luo, B.S.

Major Advisor _____
Steven L. Suib

Associate Advisor _____
S. Pamir Alpay

Associate Advisor _____
Mu-Ping Nieh

Associate Advisor _____
Alfredo Angeles-Boza

Associate Advisor _____
Stephen O. Hay

University of Connecticut
2016

Dedicated to My Family

ACKNOWLEDGEMENTS

I am sincerely thankful to my major advisor Dr. Steven L. Suib, for his advice, encouragement, and support throughout my graduate studies. His guidance and suggestions are always inspirational to my research. What I learned from Dr. Suib is not only how to be a good researcher, but also how to be a better person with responsibility and positive attitude. I would also like to express my gratitude to my associate advisors, Drs. S. Pamir Alpay, Mu-Ping Nieh, Alfredo Angeles-Boza, and Steven O. Hay for their generous help in completing this dissertation. I greatly appreciate Dr. Frank Galasso for all his help during my Ph.D. life. And of course, Mrs. Bonnie Suib, your suggestions and wonderful words will always encourage me.

I'm also grateful to my colleagues for their generous contributions and suggestions to my research and life. Working and studying in the Suib group have been a wonderful and unforgettable experience. My deep gratitude to my colleagues Dr. Altug Poyraz, Ran Miao Dr. Yashan Zhang, Dr. Chung-Hao Kuo, Dr. Hui Huang, Ting Jiang, Sheng-Yu Chen, Dave Kriz, Wei Zhong, Dr. Jacqui Cloud, Curtis Guild, Junkai He, Tahereh Jafari, Jing Jin, Ehsan, Dr. Lakshitha Pahalagedara, Dr. Madhavi Pahalagedara and everyone in Suib's group.

My grateful thanks to my Mom, Dad, and fiancé. Your unconditional love is my motivation to move forward. Without your support, I would not have made it this far. Last, thanks to GeGe, thanks for not giving up in all those hard times.

TABLE OF CONTENTS

LIST OF FIGURES

LIST OF SCHEMES

LIST OF TABLES

CHAPER 1. INTRODUCTION

1.1. Overview

In recent years, environmental and energy concerns have attracted a great deal of attention on catalytic systems. The uses of heterogeneous catalysis in environmental remediation and developing sustainable energy are increasing every year. The focus is not only on improving the catalytic activity, but also on developing simple and facile ways to prepare catalysts. By eliminating the use of expensive materials, such as noble metal (Pt, Au, Pd et al.) catalysts, simplifying the synthesis steps, and reducing side products. Heterogeneous catalysis is expected to provide improved performance in this decade.

There has been widespread studies of transition metal oxide (TMOs) materials in recent years. The TMO materials show excellent catalytic abilities in various catalytic systems. They are cheap, abundant, and most of them are environmentally friendly. The physical and chemical stabilities allow them to be used in both gas phase and liquid phase reactions. Most importantly, the physical and chemical properties such as morphology, particle sizes, oxidation states, and crystal structures of TMO materials are easy to alter via controlling material preparation methods. The resulting improved properties further leads to enhanced catalytic activity.

Among TMO materials, mesoporous TMO materials have attracted a great deal of attention since the first discovery of mesoporous materials by Mobil in 1992.[1] The huge interest of mesoporous materials is due to the easy modification of their intrinsic properties

such as pore size, pore shape, pore volume, and different mesostructures. Via controlling of these structural parameters, various catalytic activities can be developed. A significant number of publications related to mesoporous materials can be found in numerous applications such as batteries, supercapacitors, photocatalysis, sensors, and energy productions.[2, 3, 4, 5]

Generally, the synthesis of mesoporous TMO materials are based on inorganic precursor interaction, self-assembly of micelles, condensation, and template removal processes. However, the direct synthesis of mesoporous TMO materials is still a challenge due to several difficulties, such as the low crystallinity of the material, the mesostructured collapsed during template removal, small surface area, and the thermal instability. To solve some of these problems, molybdenum oxide and titanium oxide materials have been studied in this thesis. The catalysts were applied to photocatalytic, organic synthetic, electrochemical, and supercapacitive systems which are separated into four different focused chapters.

1.2. Background and Significance

1.2.1. Crystalline Mixed Phase (Anatase/Rutile) Mesoporous Titanium Dioxides for Visible Light Photocatalytic Activity

Titanium dioxide (TiO_2) has been regarded as an excellent photocatalyst compared to the other semiconductors, such as WO_3, ZnO, Fe_2O_3, and MnO_2.[6–9] The high photocatalytic activity of TiO_2 is attributed to the production of excited electrons in the conduction band

and holes in the valence band of the material to form highly reactive radical species.[10,11] In addition, titania is inexpensive, non-toxic, and has long-term stability against photo and chemical corrosion.[12] Titanium dioxide mainly occurs in three phases, anatase, rutile, and brookite. The metastable anatase and brookite phases transform irreversibly to the thermodynamically stable rutile phase upon heating treatment in the range of 400-1200 °C.[13] The photocatalytic activities of anatase and rutile phases TiO_2 materials have been widely studied. With appropriate band gaps (anatase = 3.2 eV, rutile = 3.0 eV), TiO_2 materials are able to be activated by light and generate electron/hole pairs to further oxidize/reduce organic compounds.

Among the reported TiO_2 materials, commercial TiO_2 (Degussa P25) is widely accepted as the benchmark because of its excellent photocatalytic activity.[14,15] P25 is a mixed phase material with 80% anatase and 20% rutile phases.[16,17] The analysis of the high photocatalytic activity of P25 was discussed in previous studies.[18] The synergistic effect between anatase and rutile phases is believed to be the reason for the enhanced photocatalytic activity.[19] Although P25 possesses a good photocatalytic activity, its photocatalytic performance is limited due to its nonporous nature, relatively low surface area, and low activity in visible light.

Here, we report a novel preparation method for crystalline, thermally stable (up to 800 °C) TiO_2 materials with tunable anatase/rutile phase compositions (0−100%) and monomodal mesoporosity. The control of the phase compositions was achieved by framework vanadium doping and various applied heat treatments. Vanadium (0% to 10%

doping) decreased the anatase−rutile transformation temperature (from 1000 to 600°C) and shifted the absorption band to the visible light region (narrowed the band gap). The mesoporous structure was preserved in mixed phase TiO_2. These materials are members of the discovered University of Connecticut (UCT) mesoporous materials family. The UCT materials are randomly packed nanoparticle aggregates and mesopores that are formed by connected intraparticle voids. The synthesis of UCT materials relies on controlling the sol−gel chemistry of inorganic sols in inverse surfactant micelles and NOx (nitric oxides) chemistry. The visible light (>400 nm) photocatalytic activity of mixed phase mesoporous titania samples was studied. The highest photocatalytic activity was obtained by mesoporous titania with 61% anatase and 39% rutile composition. The catalyst can totally remove (100% conversion) methylene blue dye (MB) under visible light irradiation in 2 h, whereas commercial P25 was only able to remove 28% under the same reaction conditions. The mixed phase mesoporous material also shows high photocatalytic activity for degrading phenol and 4-chlorophenol under visible light irradiation. Moreover, the good crystallinity, high surface area (94 m^2/g), and monomodal mesoporosity (around 5 nm) can be preserved even after three cycles of photocatalytic reactions.

1.2.2. Structure-Property Relationship of Copper Modified mesoporous TiO_2 Materials on Alkyne Homocoupling Reactions

Carbon-carbon triple bond compounds occur widely in nature. Among them, diyne derivatives are a very important class of compounds that with significant antibacterial, anti-HIV, anticancer, and anti-inflammatory biological activities.[20] In particular, 1,3-Diynes

they have a rod-like molecular shape and high rigidness, which play important roles in the construction of molecular complexes and serve as connectors to build up conjugated polymers, liquid crystals, and nonlinear optic materials, *etc*.[21,22]

No homocoupling reaction proceeded with only bulk copper oxide such as CuO and Cu_2O.[23] Highly dispersed copper species is indispensable for high catalytic homocoupling activity. Therefore, an appropriate support that facilitates the dispersion of copper species is necessary for the homocoupling catalytic system. Titanium dioxide (TiO_2) is one of the most studied metal oxide supports for heterogeneous catalytic systems.[24,25] TiO_2 is cheap, environmentally friendly, and can be easily incorporated with other elements.[26] Mesoporous TiO_2 has high specific surface area, uniform pore-size distribution in the targeted range and chemical stability. These attributes make TiO_2 a promising candidate to serve as a support in the homocoupling catalytic system. Moreover, the strong interactions between TiO_2 and the incorporated elements (such as Au, Cu, and Pt), prevent the surface agglomeration and enhance the dispersion of incorporated species.[27]

Thus, in this study, the copper modified TiO_2 materials prepared via three different methods to achieve different Cu species were studied. The incorporation of copper changed the physical and chemical properties of TiO_2 structure and further produces different homocoupling catalytic activities. As a result, the copper doped TiO_2 sample shows the highest activities with a yield larger than 99 %. A possible mechanism was proposed in this study. With discussions, the high catalytic activity is attributed to the large surface area, large pore size, and the Cu (I) species.

1.2.3. Mesoporous, Blue MoO_{3-x} Material as Efficient Electrocatalyst for Hydrogen Evolution Reaction

Hydrogen has been intensively pursued as a future energy carrier due to its renewable and environmentally friendly properties compared to other fuels (coal, gasoline, methane, etc.). Particularly, growing attention has paid to sustainable hydrogen evolution reaction (HER) from the water splitting reaction, which is a clean and environmentally benign reaction pathway. Usually, HER in acidic media requires lower overpotential, which is more economically efficient compared to alkaline media. Alkaline media are still promising due to the possibility for driving the overall water splitting reaction by producing hydrogen at the cathode and oxygen at the anode simultaneously.[28,29]

This study introduces a unique approach for the synthesis of non-stoichiometric, mesoporous molybdenum oxide (MoO_{3-x}) with nano-sized crystalline walls by using soft template (PEO-*b*-PS) synthesis methods. The as-synthesized mesoporous MoO_{3-x} is very active and stable (durability > 11 h) for electrochemical hydrogen evolution reaction (HER) in both acidic and alkaline conditions. The intrinsic MoO_3 serves as an HER electrocatalyst without the assistance of carbon materials, noble metals, or MoS_2 materials, which are widely used in previously developed HER systems. The results from transmission electron microscopy and N_2 sorption techniques show that the as-synthesized mesoporous MoO_{3-x} has large accessible pores (20-40 nm), which are able to facilitate mass transport and charge transfer during HER. In terms of X-ray diffraction, X-ray photoelectron spectroscopy, and diffusive reflectance UV-vis spectroscopy, the mesoporous MoO_{3-x} exhibits mixed

oxidation states (Mo^{5+}, Mo^{6+}) and an oxygen-deficient structure. The as-synthesized MoO_{3-x} only requires a low overpotential (0.12 V) to achieve 10 mA/cm^2 current density and the Tafel slope is as low as 43 mV/dec. With further studies, density functional theory (DFT) calculations demonstrated the change of electronic structure and the possible reaction pathway of HER. Oxygen vacancies and mesoporosity served as key factors for excellent performance.

1.3. References

(1) Kresge, C. T.; Leonowicz, M. E.; Roth, W. J.; Vartuli, J. C.; Beck, J. S. *Nature* **1992**, *359*, 710–712.

(2) Deng, Y.; Yu, T.; Wan, Y.; Shi, Y.; Meng, Y.; Gu, D.; Zhang, L.; Huang, Y.; Liu, C.; Wu, X.; Zhao, D. *J. Am. Chem. Soc.* **2007**, *129*, 1690–1697.

(3) Brezesinski, T.; Wang, J.; Tolbert, S. H.; Dunn, B. *Nat. Mater.* **2010**, *9*, 146–151.

(4) Chen, D.; Huang, F.; Cheng, Y.-B.; Caruso, R. A. *Adv. Mater.* **2009**, *21*, 2206–2210.

(5) Wang, D.; Choi, D.; Yang, Z.; Viswanathan, V. V.; Nie, Z.; Wang, C.; Song, Y.; Zhang, J.-G.; Liu, J. *Chem. Mater.* **2008**, *20*, 3435–3442.

(6) Cross, W. B.; Parkin, I. P.; O'Neill, S. A.; Williams, P. A.; Mahon, M. F.; Molloy, K. C. *Chem. Mater.* **2003**, *15*, 2786–2796.

(7) Xu, L.; Hu, Y.-L.; Pelligra, C.; Chen, C.-H.; Jin, L.; Huang, H.; Sithambaram, S.; Aindow, M.; Joesten, R.; Suib, S. L. *Chem. Mater.* **2009**, *21*, 2875–2885.

(8) Shi, Y.; Li, H.; Wang, L.; Shen, W.; Chen, H. *ACS Appl. Mater. Interfaces* **2012**, *4*, 4800–4806.

(9) Cao, H.; Suib, S. L. *J. Am. Chem. Soc.* **1994**, *116*, 5334–5342.

(10) Liu, S.; Yu, J.; Jaroniec, M. *J. Am. Chem. Soc.* **2010**, *132*, 11914–11916.

(11) Macak, J. M.; Zlamal, M.; Krysa, J.; Schmuki, P. *Small* **2007**, *3*, 300–304.

(12) Yu, J. C. *Chem. Mater.* **2002**, *14*, 3808–3816.

(13) Ohtani, B.; Prieto-Mahaney, O. O.; Li, D.; Abe, R. *J. Photochem. Photobiol. A Chem.* **2010**, *216*, 179–182.

(14) Jafry, H. R.; Liga, M. V; Li, Q.; Barron, A. R. *Environ. Sci. Technol.* **2011**, *45*, 1563–1568.

(15) Pfeifer, V.; Erhart, P.; Li, S.; Rachut, K.; Morasch, J.; Brötz, J.; Reckers, P.; Mayer, T.; Rühle, S.; Zaban, A.; Mora Seró, I.; Bisquert, J.; Jaegermann, W.; Klein, A. *J. Phys. Chem. Lett.* **2013**, *4*, 4182–4187.

(16) Hurum, D. C.; Gray, K. A.; Rajh, T.; Thurnauer, M. C. *J. Phys. Chem. B* **2005**, *109*, 977–980.

(17) Hurum, D. C.; Agrios, A. G.; Gray, K. A.; Rajh, T.; Thurnauer, M. C. *J. Phys. Chem. B* **2003**, *107*, 4545–4549.

(18) Liu, Z.; Zhang, X.; Nishimoto, S.; Jin, M.; Tryk, D. A.; Murakami, T.; Fujishima, A. *Langmuir* **2007**, *23*, 10916–10919.

(19) Serpone, N. *J. Phys. Chem. B* **2006**, *110*, 24287–24293.

(20) Shi Shun, A. L. K.; Tykwinski, R. R. *Angew. Chem. Int. Ed. Engl.* **2006**, *45*, 1034–1057.

(21) Gleiter, R.; Werz, D. B. *Chem. Rev.* **2010**, *110*, 4447–4488.

(22) Liu, J.; Lam, J. W. Y.; Tang, B. Z. *Chem. Rev.* **2009**, *109*, 5799–5867.

(23) Oishi, T.; Katayama, T.; Yamaguchi, K.; Mizuno, N. *Chemistry* **2009**, *15*, 7539–7542.

(24) Shiraishi, Y.; Sakamoto, H.; Sugano, Y.; Ichikawa, S.; Hirai, T. *ACS Nano* **2013**, *7*, 9287–9297.

(25) Si, R.; Tao, J.; Evans, J.; Park, J. B.; Barrio, L.; Hanson, J. C.; Zhu, Y.; Hrbek, J.; Rodriguez, J. A. *J. Phys. Chem. C* **2012**, *116*, 23547–23555.

(26) Khakpash, N.; Simchi, A.; Jafari, T. *J. Mater. Sci. Mater. Electron.* **2011**, *23*, 659–667.

(27) Benaskar, F.; Engels, V.; Rebrov, E. V; Patil, N. G.; Meuldijk, J.; Thüne, P. C.; Magusin, P. C. M. M.; Mezari, B.; Hessel, V.; Hulshof, L. A.; Hensen, E. J. M.; Wheatley, A. E. H.; Schouten, J. C. *Chemistry* **2012**, *18*, 1800–1810.

(28) McCrory, C. C. L.; Jung, S.; Peters, J. C.; Jaramillo, T. F. *J. Am. Chem. Soc.* **2013**, *135*, 16977–16987.

(29) Suntivich, J.; May, K. J.; Gasteiger, H. A.; Goodenough, J. B.; Shao-Horn, Y. *Science* **2011**, *334*, 1383–1385.

CHAPER 2. CRYSTALLINE MIXED PHASE (ANATASE/RUTILE) MESOPOROUS TITANIUM DIOXIDES FOR VISIBLE LIGHT PHOTOCATALYTIC ACTIVITY

2.1. Introduction

In recent years, environmental concerns have increased the focus on the synthesis of heterogeneous photocatalysts for decomposition of organic contaminants in the environment under light (UV and visible) irradiation. Titanium dioxide is the most widely studied photocatalyst among all the transition metal oxide materials which are cheap, abundant, environmentally friendly, and highly stable in harsh media. The high surface area and nanocrystallinity of mesoporous materials qualify them as excellent candidates as active photocatalysts. The mesoporous TiO_2 material was first synthesized by Antonelli et al. in 1995.[1] Since then, numerous mesoporous TiO_2 materials have been reported with tunable mesoporosity and high surface area, as high as 1200 m^2/g.[2–7] High photocatalytic activity of these materials is favored by nanocrystalline walls, which allow photogenerated electrons and holes to reach the surface easily.

However, the major drawbacks of mesoporous TiO_2 materials are their low thermal stability and poorly ordered structure. Generally, the mesoporous TiO_2 materials prepared by soft templating methods (involves surfactant micelles) lose their mesoporosity at temperatures above 400°C.[8] Moreover, they mostly only possess the anatase phase. The photocatalytic activity of mesoporous materials can be improved by using dopants (e.g. B,

Ag, W), which promote the charge separation efficiency and narrow the band gap energy to achieve and improve the visible light photocatalytic activity.[9,10]

Vanadium as a dopant extends the band gap of TiO_2 to the visible light region (> 400 nm).[11,12] The extension is achieved by forming intermediate energy levels. Vanadium, as a dopant, is also known to promote the phase transformation of TiO_2 from anatase to rutile.[13] Pure TiO_2 undergoes an anatase to rutile phase transformation in the range of 400-1200°C depending on preparation methods.[14–16] Vanadium doping can decrease the transition temperature as much as 450°C (from 1100°C to 650°C).[17] In this study, we report the synthesis of vanadium doped mesoporous anatase/rutile mixed phase TiO_2 materials. The anatase/rutile ratio of the material can be tuned by varying the dopant concentration and the heat treatment. The materials maintain the unique mixed phase nature by preserving the mesoporous structure. Combining all these advantages, these mesoporous photocatalysts exhibited outstanding adsorption capacity (up to 80%) and high visible light photocatalytic activity (~100%).

2.2. Experimental Section

2.2.1. Preparation of the Catalysts

In a typical synthesis, 0.01 mol (2.84 g) of titanium isopropoxide was dissolved in a solution containing 0.094 mol (7 g) of 1-butanol, 0.016 mol (1 g) of HNO_3 and 1.72×10^{-4} mol of P123 surfactant in a 150 mL beaker at room temperature (RT) under magnetic stirring to obtain a clear gel. In a separate container, a vanadium source was prepared by

dissolving 0.06 mol (14.64 g) of vanadium oxytriisopropoxide in 250 mL of 1-butanol. X mL (X=0.416, 2.08, 4.16 mL) of vanadium solution was slowly added to the titanium gel under magnetic stirring to obtain 1%, 5% and 10% vanadium loading (vanadium%= (mol V/mol Ti)×100%). The obtained clear gel was dark yellow in appearance and placed in an oven running at 120°C for 4 h. For all doped samples, the obtained dark orange， transparent (rigid) films were calcined in a tubular furnace under Ar at various temperatures (600-800°C, 1°C/min) for 2 h. Followed by a second heat treatment under air at 450°C for 2 h. The doped samples are labeled as M%V-Ti-Y, where M is the mol% of vanadium (M=1, 5, 10%) and Y is the calcination temperature under Ar. For undoped samples, the obtained dark orange, transparent (rigid) films were calcined under air for 4 h at various temperatures (600-1000°C) and labeled as 0%V-Ti-Z (600 - 1000 °C). 0%V-Ti-450 is an undoped sample calcined under air at 450°C for 4 h.

2.2.2. Catalysts Characterization

Powder X-ray diffraction (PXRD) analyses were performed on a Rigaku Ultima IV diffractometer (Cu Kα radiation, λ=1.5406 A) with an operating voltage of 40 kV and a current of 44 mA. Raman spectra were taken on a Renishaw 2000 Raman microscope with a wavelength of 514 nm, exposure time of 16 , and accumulations of 4 times. Nitrogen (N_2) sorption experiments were conducted on a Quantachrome Autosorb-1-1C automated sorption system. The powders were degassed at 200°C for 4 h prior to the measurements. The surface areas were calculated by the Brunauer-Emmett-Teller (BET) method and the pore size distributions were calculated by the Barrett-Joyner-Halenda (BJH) method from

the desorption isotherm. Morphological characterization was done using an FEI Nova NanoSEM 450 with an accelerating voltage of 2.0 kV. Diffuse reflectance ultraviolet-visible (DR UV-vis) spectra of the powder samples were collected with a diffuse reflectance apparatus attached to a Shimadzu UV-2450 ultraviolet-visible spectrophotometer. The powder samples were diluted in barium sulfate and pressed into the sample holder. X-ray photoelectron spectroscopy (XPS) measurements were performed in a PHI model 590 spectrometer with multiprobes (ΦPhysical Electronics Industries Inc.), using Al Kα radiation (λ=1486.6 eV) operated at 250 W. The shift of binding energy due to relative surface charging was corrected using the C 1s level at 284.6 eV as an internal standard. Transmission electron microscopy (TEM), high resolution transmission electron microscopy (HRTEM), and selected area electron diffraction (SAED) were obtained in a JEOL 2010 UHR FasTEM operating at an accelerating voltage of 200 kV. The samples were prepared by dispersing the material in methanol. A drop of the dispersion was placed on a carbon coated copper grid and allowed to dry under ambient conditions. FTIR spectra of the pellets were collected using a SpectraLab Scientific Nicolet Magna 560 spectrometer. Thirty two scans were collected with a 4 cm^{-1} spectral resolution.

2.3. Results

2.3.1. Phase Transformation and Compositions

Figure 2.1a shows the PXRD patterns of undoped TiO_2 (0%V-Ti-Z) samples calcined under different temperatures (600-1000°C). Up to 900°C, the material displays the pure

anatase phase. The rutile phase related diffraction lines started to appear above 900°C. After vanadium was introduced into the TiO_2 system, much lower transformation temperatures were achieved compared to undoped TiO_2 (0%V-Ti-Z). All diffraction lines can be assigned either anatase or rutile phases and no vanadium oxide related diffraction lines were observed. For the 1%V-Ti-Y samples (Figure 2.1b), the rutile phase related diffraction lines can be observed at 900°C and the rutile phase became the dominant phase at 1000°C. When the vanadium dopant concentration increased to 5% (5%V-Ti-Y) (Figure 2.1c), the anatase-rutile transformation temperature decreased to 800°C. A further increase in the vanadium dopant concentration to 10% (Figure 2.1d) resulted in an anatase-rutile transformation temperature decrease even more to 700°C. In Figure 2.1e, the Raman spectrum of 0%V-Ti-450 sample depicts the typical anatase vibrational modes, which are 143, 198, 395, 515, and 636 cm^{-1}.[18] All Raman peaks of the M%V-Ti-Y samples can be identified as either anatase or rutile, with no corresponding vanadium oxide peaks. The samples calcined at 700°C (M%V-Ti-700) display fundamental vibrational modes of the anatase phase. However, a clear broadening of peaks can be observed between 5%V-Ti-700 and 10%V-Ti-700. Both 5%V-Ti-800 and 10%V-Ti-800 samples showed peaks at 446 and 609 cm^{-1}. These vibrational modes can be identified as the most intense rutile vibrational modes.[19]

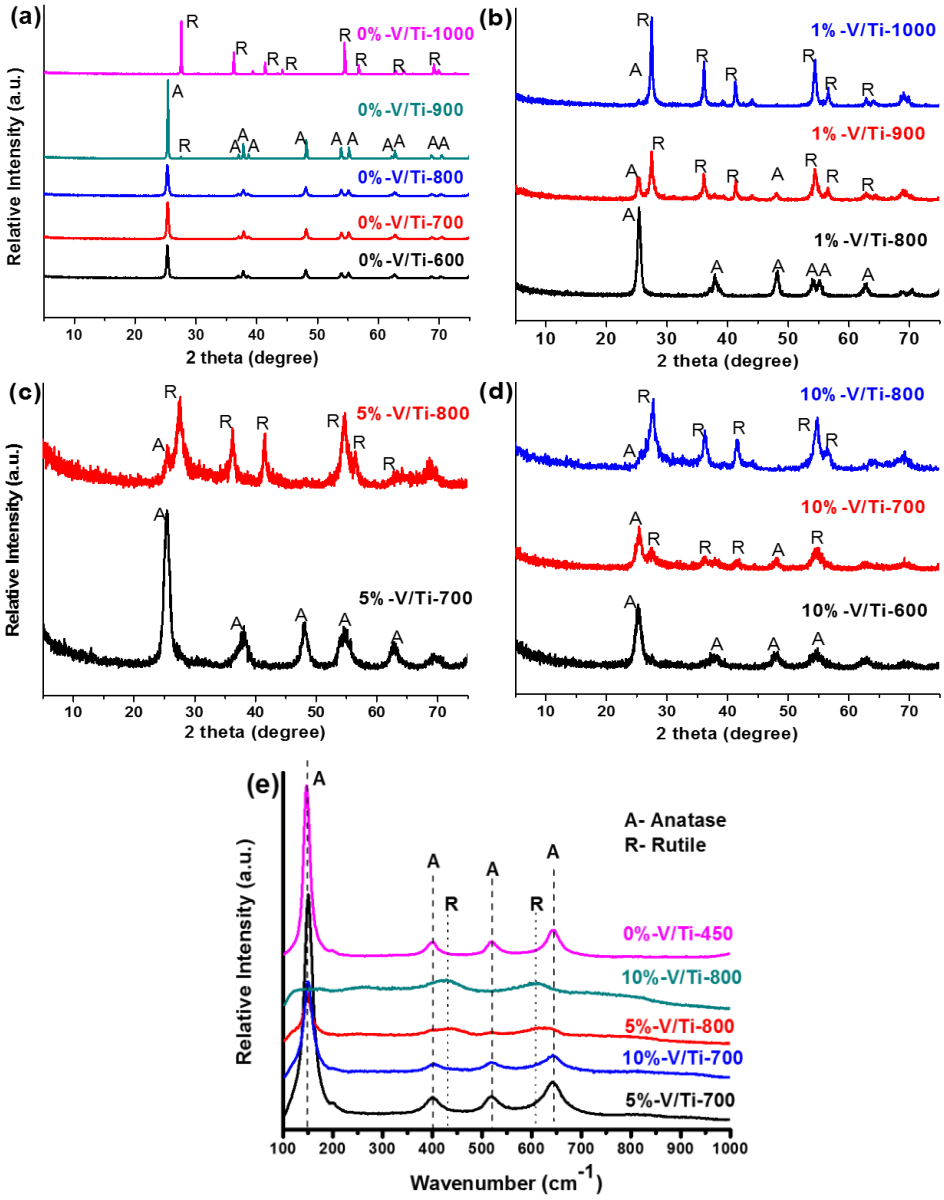

Figure 2. 1 PXRD patterns of (a) Undoped TiO_2 (0%V-Ti-Z) calcined under air at 600~1000°C. (b) 1% vanadium doped TiO_2 samples (1%V-Ti-Y) calcined at 800~1000°C. (c) 5% vanadium doped TiO_2 samples (5%V-Ti-Y) calcined at 700~80 °C. (d) 10% vanadium doped TiO_2 samples (10%V-Ti-Y) calcined at 600~800°C. A and R stand for typical anatase and rutile diffractions, respectively. (e) Raman spectra for undoped TiO_2 sample (0%V-Ti-450) which is in pure anatase phase and all mixed phase TiO_2 samples (M%V-Ti-Y).

2.3.2. Mesostructure and Pore Size Distributions

Figure 2.2 shows N_2 sorption isotherms along with the BJH pore size distributions. 5%V-Ti-700 has a surface area of 75 m^2/g and 5%V-Ti-800 has a surface area of 76 m^2/g. The 10%V-Ti-700 possesses the highest surface area (94 m^2/g). The surface area decreased to 50 m^2/g, when the calcination temperature was increased to 800°C (10%V-Ti-800). The decrease in surface area may be due to the high proportion of rutile. The other possibility is the partial loss of mesoporosity. Figures 2.2a-b display the N_2 sorption isotherms for 5%V-Ti-700 and 10%V-Ti-700 samples, respectively. Both isotherms show Type IV adsorption isotherms along with a Type I hysteresis loop, which indicates the presence of regular cylindrical mesoporosity.[20] BJH desorption pore size distributions are 3.8 nm for 5%V-Ti-700 and 5.6 nm for 10%V-Ti-700. In Figure 2.2c-d, 5%V-Ti-800 and 10%V-Ti-800 samples display a late adsorption edge ($P/P_0>0.8$) suggesting an increase in pore size. The two step hysteresis loop of 5%V-Ti-800 indicates either a bimodal pore size distribution or plugs within the pore structure.[21,22] Moreover, 10%V-Ti-800 exhibits a smooth desorption branch leading to a monomodal pore size of 17 nm.

All results of TEM were collected from the 10%V-Ti-700 sample. In Figure 2.3a, the area shows aggregated nanoparticles with a mean size of ~10 nm, in which the measured *d*-spacing (0.35 nm) corresponds to the (101) planes of the anatase phase. Some areas of this material shows larger particle sizes (~50 nm) and larger pores (Figure 2.3b). The particles display lattice spacings of 0.32 nm which could be assigned to the interplanar distance of the (110) planes of the rutile phase. Further observation by SAED (inset image

in Figure 2.3b) confirmed that the nanoparticles have the rutile structure and higher degrees of crystallinity compared to the anatase region. Although the rutile regions present the largest particle sizes, the porosity was retained, which correlates with the bimodal pore size distribution obtained from N_2 sorption analyses.

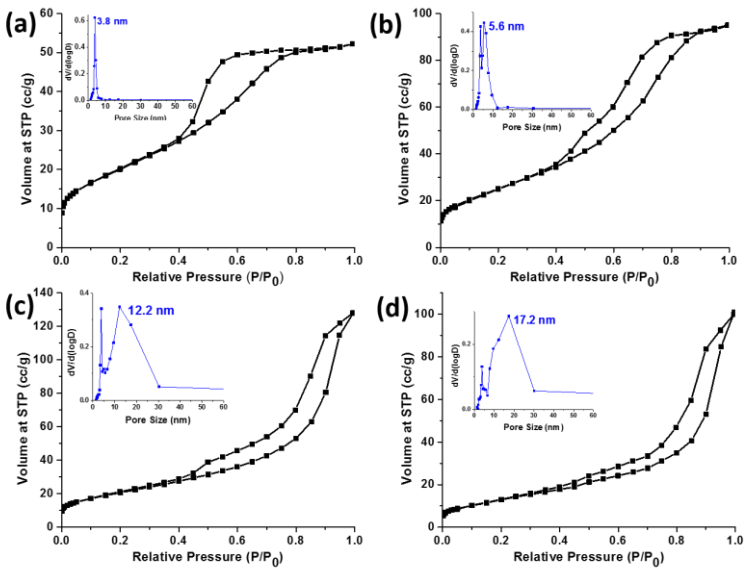

Figure 2. 2 N_2 sorption isotherms for (a) 5%V-Ti-700, (b) 10%V-Ti-700, (c) 5%V-Ti-800, (d) 10%-V/Ti-800 samples. The inset figures are the BJH desorption pore-size distributions for each sample (a) 3.8 nm, (b) 5.6 nm, (c) 12.2 nm, (d) 17.2 nm.

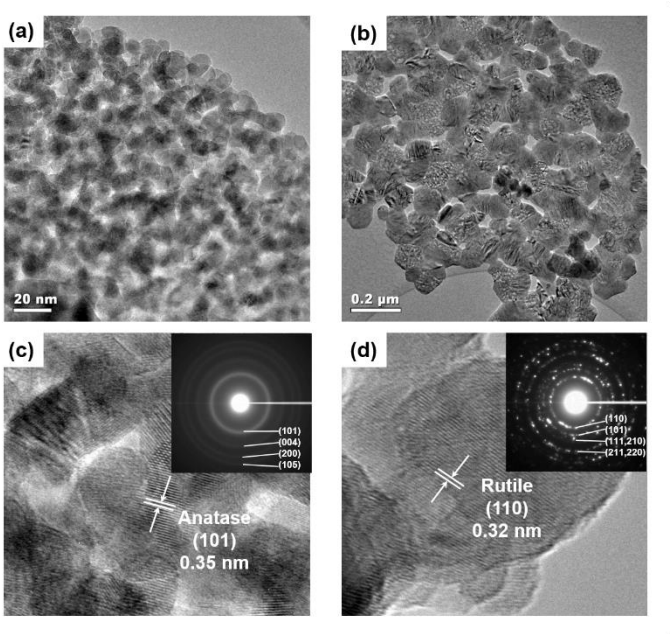

Figure 2. 3 Low magnification HRTEM images of sample 10%V-Ti-700 from different domains, (a) anatase phase domain, (b) Rutile phase domain. (c) High magnification HRTEM images of anatase domain with (101) interplanar distance of 0.35 nm. (d) High magnification HRTEM images of rutile domain with (110) interplanar distance of 0.32 nm. Selected area electron diffraction images (inset) of rutile domain show higher crystallinity than the anatase domain.

2.3.3. Absorption Property and Surface Oxidation States

Figure 2.4a presents the DR UV-vis results of M%V-Ti-Y samples. Undoped TiO_2 (0%V-Ti-450) reveals a cut-off wavelength around 400 nm as expected in the UV range.[23] All doped TiO_2 samples exhibit a red shift as compared to undoped TiO_2 (0%V-Ti-450). The tailing of absorption curves shows that all doped samples (M%V-Ti-Y) are able to absorb photon energies greater than 400 nm which are in the visible range. No separate V_2O_4 or V_2O_5 peaks were observed in the recorded DR UV-vis spectra, which have major peaks at ~476, 338 nm and 355, 240 nm, respectively. [24,25]

The X-ray Photoelectron Spectroscopy (XPS) of all M%V-Ti-Y samples are shown in Figure 2.5 for (a) Ti 2p, (b) O 1s and (c) V 2p spectral regions. The binding energies of the 0%V-Ti-450 sample (Figure 2.5a) for Ti 2p core levels, found at 458.7 eV and 464.4 eV correspond to Ti $2p_{3/2}$ and Ti $2p_{1/2}$ levels, respectively.[26,27] Compared to the 0%V-Ti-450 sample, the Ti 2p peaks of all M%V-Ti-Y samples get broader which may be due to higher calcination temperatures (influence of the particle size) and the framework replacement of titanium with vanadium. The O 1s peaks are broad and asymmetric (Figure 2.5b) in which curve fitting was achieved using three component peaks. These three peaks can be identified as follows: (1) peaks in the 529.5-530.5 eV range can be assigned to "O^{2-}" ions in the lattice (blue curve); (2) peaks in the range of 531-532 eV can be assigned to adsorbed OH^- species, O^- species, or oxygen vacancies (red curve); (3) peaks in the range of 532.5-533.5 eV can be assigned to adsorbed molecular water (green curve).[28] The significantly increased surface adsorbed hydroxyl groups may enhance the photocatalytic activity of the

samples.[29] The peaks of vanadium are V $2p_{3/2}$ and V $2p_{1/2}$ levels (Figure 2.5c). Since O 1s satellite peaks interfere with the V $2p_{1/2}$ region significantly, only V $2p_{3/2}$ will be discussed. The binding energy peaks at 517.5±0.1 eV and 516.3±0.1 eV contribute to V^{5+} (red curve) and V^{4+} (blue curve), respectively.[30] The green curve at 520 eV corresponds to the O 1s satellite.[31] The results of curve fitting in Figure 2.5c suggest that all samples contain V^{5+} species. Moreover, one can clearly observe a shoulder in the 5%V-Ti-700, 10%V-Ti-700, and 10%V-Ti-800 samples, which can be assigned to the V^{4+} species. In the 5%V-Ti-800 sample the obvious shoulder is missing. This may indicate that only V^{5+} species exist in this sample. V^{5+} is an expected state, since we used a vanadium (V) oxytriisopropoxide as the precursor. The formation of V^{4+} is probably due to reduced V^{5+} or oxygen vacancies generated during the calcination steps. The reduction of vanadium from V^{5+} to V^{4+} further affected Ti^{4+} ions in the lattice, decreasing electron density of Ti^{4+}, which can explain the shift to higher binding energy values of the Ti 2p peak in Figure 2.5a. The specific binding energies of all V 2p and O 1s levels and the compositions of surface species are listed in Table 2.1.

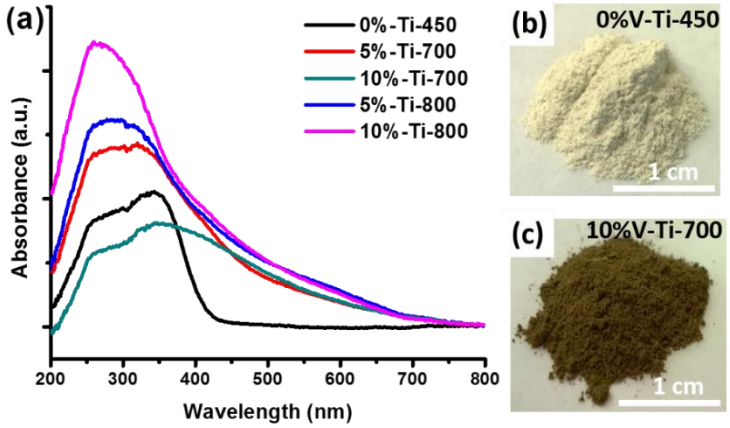

Figure 2. 4 (a) DR UV-vis spectra for all vanadium doped mixed phase samples (M%V-Ti-Y) and undoped TiO_2 sample (0%V-Ti-450) with pure anatase phase. (b) Photo for 0%V-Ti-450 and (c) photo for 10%V-Ti-700 samples. Color changed significantly after introduce vanadium into the TiO_2 lattice.

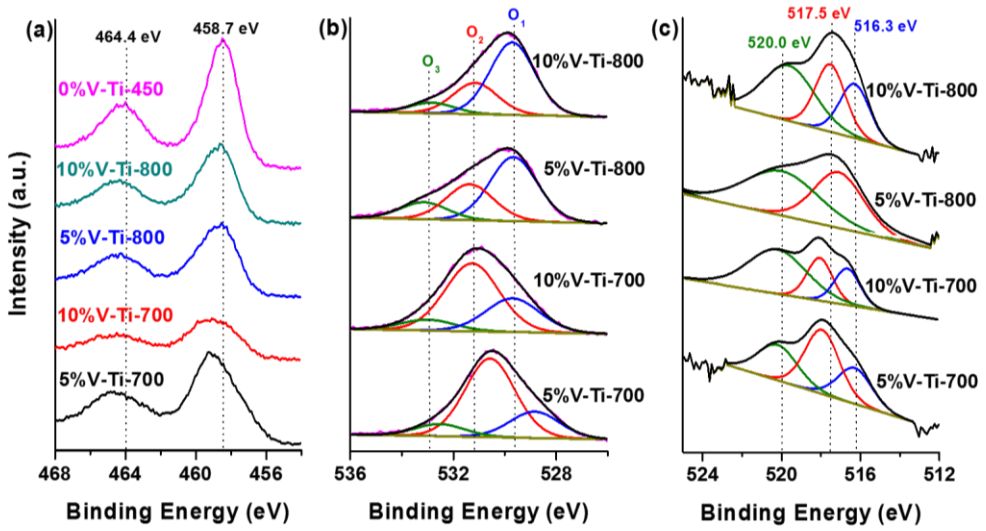

Figure 2. 5 XPS spectra details for (a) Ti 2p binding energy regions, Ti $2p_{3/2}$ at 458.7 eV and Ti $2p_{1/2}$ at 464.4 eV. (b) O 1s level, blue curve (O_1) exhibits type 1 oxygen: lattice oxygen; red curve (O_2) exhibits type 2 oxygen: surface adsorbed oxygen species (e.g., OH^-, O^- species); green curve (O_3) exhibits type 3 oxygen: surface adsorbed molecular water. (c) V $2p_{3/2}$ binding energy region for all vanadium doped mixed phase samples (M%V-Ti-Y), blue curve around 516.3 eV correspond to V^{4+} species; red curve around 517.5 eV correspond to V^{5+} species; green curve around 520.0 eV correspond to the O 1s satellite.

Table 2.1 Binding energy of the XPS V 2p, O 1s core levels and the compositions of surface species.

Sample	V 2p core levels (eV)		O 1s core levels (eV)		
	V^{4+}	V^{5+}	O^{2-}	OH^-/O^-	H_2O
5%V-Ti-700	516.4	518.0	529.0	531.0	532.8
10%V-Ti-700	516.6	518.0	529.5	531.2	533.0
5%V-Ti-800	/	517.1	529.5	531.3	533.3
10%V-Ti-800	516.3	517.5	529.7	531.2	533.0

2.3.4. Adsorption ability and Photocatalytic Activity

Prior to the photocatalytic degradation studies, the adsorption ability of the samples were investigated by performing all the degradation reactions in the dark (Figure 2.6a). P25 did not show any obvious adsorption ability (6%) even after 120 min. Compared to P25, all M%V-Ti-Y samples have higher adsorption abilities (>45%). Figure 2.6b displays the results of MB degradation under visible light irradiation. The best performance was achieved by the 10%V-Ti-700 sample, since all MB dye was removed after 120 min of irradiation. The other mixed phase samples showed similar catalytic performances (Figure 2.6b); ~70% of the MB was decomposed after 120 min.

To further understand the photocatalytic performance of mixed phase mesoporous TiO_2 and its mechanism, sample 10%V-Ti-700 was used to degrade solutions of phenol and 4-chlorophenol (Figure 2.6c-d). Experiments were first conducted in the dark for 30 min to achieve adsorption equilibrium. No obvious adsorption of phenol or 4-chlorophenol were observed on the surface of 10%V-Ti-700 or P25. After visible light was turned on, 10%V-Ti-700 is able to remove around 40% phenol (red curve in Figure 2.6c) and 50% 4-chlorophenol (red curve in Figure 2.6d) in 3 h. P25 (blue curves in Figure 2.6c-d) shows no significant degradation for phenol or 4-chlorophenol in 3 h. Blank control experiments were operated under the same conditions without any catalyst (green curves in Figure 2.6c-d). Phenol and 4-chlorophenol are quite stable under light irradiation without any catalyst treatment.

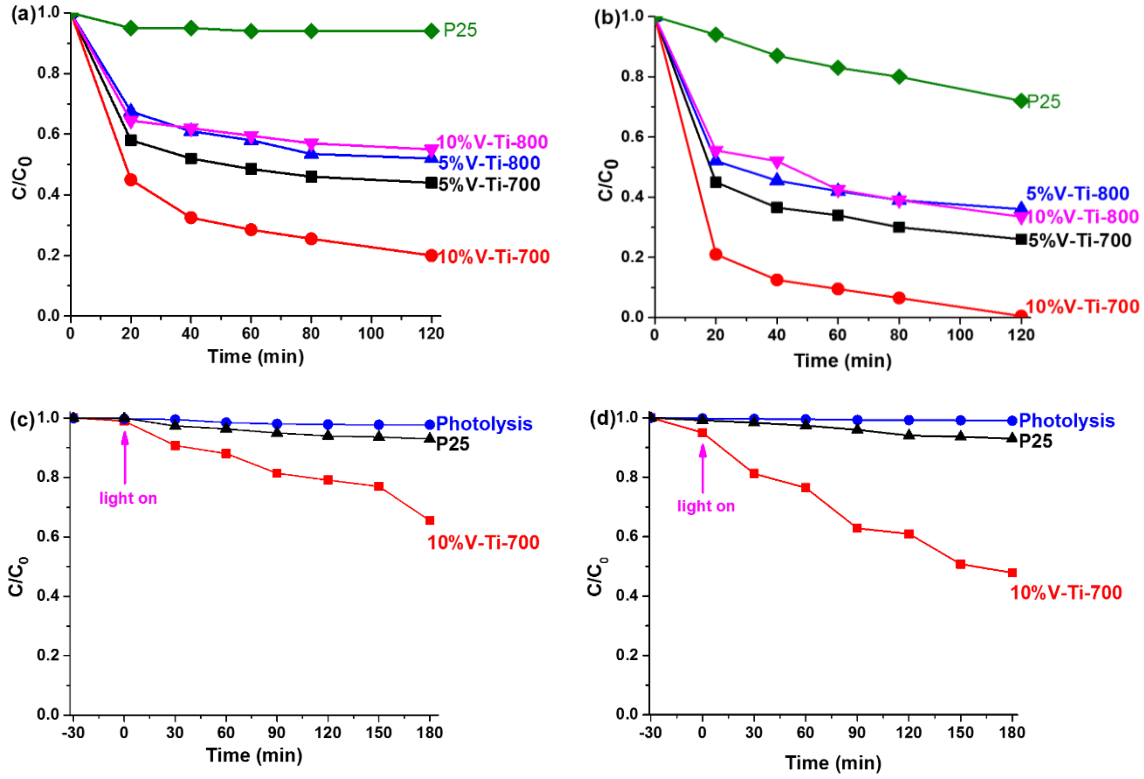

Figure 2. 6 (a) Adsorption ability tests for all mixed phase TiO2 samples (M%V-Ti-Y) by using 100 mg of catalysts adsorbing 100 mL, 10-4M MB dye under dark for 2 h, P25 as a comparison. (b) Photocatalytic decomposition of 100 mL,10-4 MB dye under visible light in 2 h by using 100 mg of 5%V-Ti-700, 10%V-Ti-700, 5%V-Ti-800, 10%V-Ti-800 and P25 samples, respectively. Photocatalytic decomposition of 100 mL, 20 ppm (c) phenol and (d) 4-chlorophenol under visible light in 3 h by using 100 mg of 10%V-Ti-700, P25 and blank control (photolysis) without any catalyst. Visible light was turned on after 30 min adsorption in the dark.

2.4. Discussion

2.4.1. Vanadium Doped Mixed Phase Mesoporous Structure

In this study, mixed phase mesoporous TiO_2 were prepared based on a recently developed sol-gel method, combined with using vanadium as a phase transformation promoter, and Ar atmosphere to retain the mesostructure. The PXRD results suggest that the anatase rutile transformation was favored by the presence of vanadium (Figure 2.1a-d). In comparison, the 0%V-Ti-Z sample requires high transformation temperatures (900-1000°C), whereas M%V-Ti (M=5,10%) was transformed at 700-800°C, indicating that vanadium may act as a phase transformation promoter.[32] No vanadium oxide related diffraction lines were observed during PXRD analysis, suggesting that either doping of vanadium into the TiO_2 lattice or well dispersed nano-oxide (polymeric form) clusters were produced on the surface of TiO_2. No vanadium oxide clusters can be detected in Raman Spectroscopy (Figure 2.1e) or TEM (Figure 2.3) analysis, which further support that vanadium may enter into the TiO_2 lattice and substitute for part of the Ti^{4+}. The small ionic radius of vanadium ($V^{2+/3+/4+/5+}$=93/78/72/68 pm) compared to titanium ($Ti^{2+/3+/4+}$=100/81/75 pm), make this substitution possible.[33] Furthermore, control samples (m%V_2O_5-TiO_2) in which vanadium oxide (V_2O_5) was physically mixed with undoped TiO_2 were studied by PXRD and Raman spectroscopy to show the differences between the vanadium doped sample and the vanadium oxide mixed sample.

The N_2 sorption results (Figure 2.2) suggest the preservation of mesoporosity during the anatase-rutile phase transformation. Generally, the mesostructure (so as the mesopores)

collapses during a high temperature calcination process due to the crystallization of the inorganic walls. However, in our study, all samples were calcined above 700°C under Ar atmosphere with surfactant supporting the pores. The retained mesopores indicate that the inert atmosphere contributes to stabilizing the framework of the mesostructure by forming a carbon support (heating under inert atmosphere converts surfactant to carbon).[8] Simultaneously, anatase was transformed to the rutile phase during high temperature calcination without destroying the mesopores.

The oxidation states of vanadium in the lattice can be determined by XPS analysis (Figure 2.5). The XPS analysis suggests that titanium mainly displayed Ti^{4+} in the structure and vanadium showed both V^{4+} and V^{5+} states. The oxidation state of the vanadium precursor is V^{5+}. The presence of V^{4+} may be due to reduced V^{5+} and oxygen vacancies generated during calcination.[34] Moreover, the surface dehydroxylation offers electrons to vanadium sites and forms stable Ti-O-V bonds during calcination.[35] Talavera et al. suggested that the size and the charge of the dopant ions both affect the anatase-rutile transformation.[36] V^{4+} can substitute for Ti^{4+} without intense lattice distortion. However, V^{5+} replaces Ti^{4+} with a charge compensation. Once vanadium enters the TiO_2 lattice, the crystallographic similarity between rutile and vanadium oxide (e.g. VO_2) provides a suitable space for the rutile phase to grow on.[37] In addition, the energy barrier for the distortion of a V-O bond is lower than for a Ti-O bond and thus vanadium doped TiO_2 can transform from anatase to rutile at lower temperatures.[38]

2.4.2. Adsorption Ability and Photocatalytic Performance

All the adsorption and photocatalytic tests were conducted on a set-up shown in Scheme 2.1. Certain amounts of catalysts were added into the quartz vessel for each experiment. In adsorption tests, no light was applied and the quartz vessels were covered with aluminum foil. In photocatalytic tests, the Xenon lamp was turned on and a bandpass filter (> 400 nm) was applied.

The unique mixed phase mesoporous structure should have significant contribution to the adsorption and photocatalytic activity. Adsorption is a prerequisite for good photocatalytic activity. Therefore, the adsorption ability of all the M%V-Ti-Y samples were conducted by MB dye adsorption under dark conditions. Compared to P25, all the M%V-Ti-Y samples showed much higher adsorption ability of MB dye (Figure 2.6a) due to their larger surface areas and mesoporous structures (Figure 2.2). Larger surface areas and pore structures can offer more active sites to adsorb bulky dye molecules and facilitate the diffusion of dye molecules inside the pores. The presence of mesopores also favor the rapid diffusion of quanta, which form during the photocatalytic reaction and further promote photogenerated charge transport to the surface and improve the separation rate.[39]

The photocatalytic efficiency of mixed phase mesoporous TiO_2 was investigated by MB dye, phenol and 4-chlorophenol degradation (Figure 2.6b) under visible light irradiation. The efficiency of most photocatalysts is determined by the recombination rate of electron/hole pairs. In this study, both the introduction of the vanadium dopant and the presence of the rutile phase contribute to the high electron/charge separation rate. Introduction of vanadium would alter the electronic properties of TiO_2. The V^{4+}/V^{5+} pair

could form an impurity energy band around 2.1 eV, which can work as an e^-/h^+ trap that improves the separation efficiency. [40] The substitution of a Ti^{4+} ion by a V^{5+} induces a free electron, which can be easily excited to the TiO_2 conduction band with light irradiation.[41] Moreover, the V^{4+} traps the photogenerated hole to form V^{5+}.[40] Therefore, the V^{4+}/V^{5+} pair acts as an electron/hole trap center, which substantially decreases the recombination rate.

The synergetic effect between anatase and rutile is another reason for high photocatalytic activity. The rutile phase TiO_2 has been reported to have a lower band gap energy than anatase TiO_2 (3.03 eV vs 3.20 eV).[42] When these two phases combined, a staggered band gap formed and the synergistic effect causes an efficient charge separation across phase junctions.[43] The direction of charge migration across the phase junction is controversial, but has widely been regarded as electrons flowing from rutile to anatase and holes moving in the opposite direction.[44,45,46] Electrons can be transferred from the rutile conduction band to the anatase conduction band and further transferred to surface sites. Similarly, photogenerated holes can be transferred from the anatase valence band to the rutile valence band and further transferred to surface sites. In our materials (M%V-Ti-Y), both the anatase and rutile phases could potentially be excited by visible light due to the impurity energy gap of V^{4+}/V^{5+} (Scheme 2.2). With visible light irradiation, electrons in the valence band adsorb enough energy so that electrons are excited to the V^{4+}/V^{5+} level or conduction band. The V^{4+}/V^{5+} level introduces electrons to the rutile conduction band. The electrons in the rutile conduction band will further migrate to the anatase conduction band (process 1) due to the staggered band alignment and then are transferred to surface

molecular oxygen to generate superoxide anion radicals. The photogenerated holes migrate to the opposite side, from the anatase valence band to the rutile valence band (process 2) and are further transferred to the surface to react with the hydroxyl species on TiO_2, to produce highly active hydroxyl radicals. The anatase and rutile proportion is also related to photocatalytic activity. In our study, among all the mixed phase TiO_2 samples, the 10%V-Ti-700 (61% anatase, 39% rutile) sample possesses the highest photocatalytic ability. Besides the mixed phase structure and vanadium impurity levels, the amount of surface adsorbed hydroxyl species is another important factor affecting the photocatalytic activity. 5%V-Ti-700 and 10%V-Ti-700 samples have better photocatalytic activities than other samples. Based on O 1s XPS spectra (Figure 2.5b), these two samples showed predominately surface adsorbed oxygen species compared to the other samples. The contribution of surface adsorbed species, like hydroxyl groups and superoxide species, cannot be ignored. The surface hydroxyl groups favor capturing holes to form $OH^{\bullet}$ and also promote O_2 adsorption to trap electrons.[47,48] More surface adsorbed oxygen may lead to higher production of radicals. The highly reactive hydroxyl radicals rapidly attack organic pollutants, effectively preventing the recombination of electrons and holes. Thus, the higher amounts of surface hydroxyl groups result in the promotion of photocatalytic activity.[49–51]

Scheme 2. 1. The experimental set-up for adsorption and photocatalytic tests.

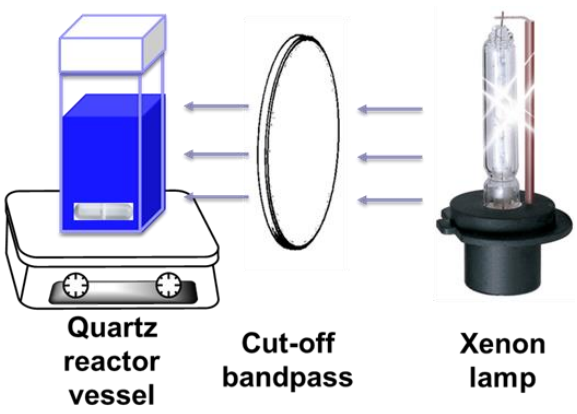

Scheme 2. 2. Mechanism for the synergistic effects of rutile and anatase. The V^{4+}/V^{5+} pair form an impurity energy band at 2.1 eV. Generation of $OH^{\cdot}$ and $O_2^{\bullet-}$ radicals by visible light (> 400 nm) activation. Photogenerated electrons excite from the valence band (VB) to the conduction band (CB) and photogenerated holes left in the VB. Process ① shows the photogenerated electrons in rutile conduction band migrate to the anatase conduction band. Process ② shows the photogenerated holes in anatase valence band migrate to the rutile valence band.

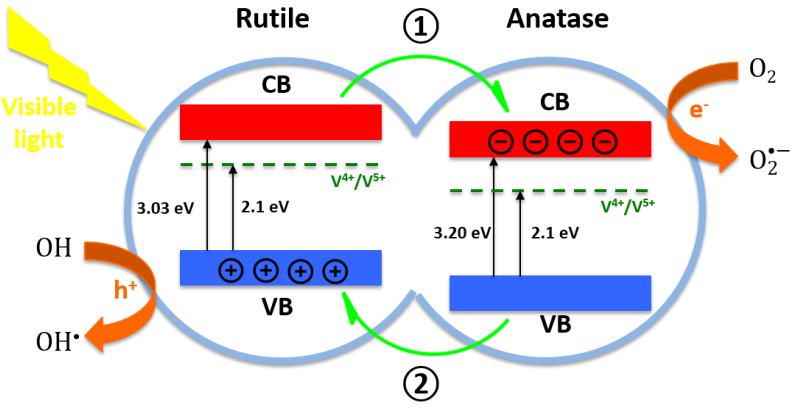

2.5. Conclusions

Thermally stable, crystalline mesoporous anatase/rutile mixed phase TiO_2 materials were first prepared by a novel sol-gel method and characterized by different techniques. By altering the concentration (0~10%) of vanadium dopant and the calcination temperature (600~1000°C), the anatase/rutile proportion (0~100%) can be easily controlled without destroying the mesopores. The inert atmosphere (Ar) contributes to stabilizing the framework of the mesostructure by forming a carbon support. Vanadium acts as an anatase-rutile transformation promoter and also favors narrowing the band gap energy of TiO_2. In addition, the synergistic effects of anatase/rutile and the mesoporous structure contribute to the enhanced photocatalytic activity. Their high adsorption abilities were studied by MB adsorption in the dark. Up to 80% MB can be adsorbed. The adsorption recovery tests further prove the amount of dye adsorbed and no intermediates were found in the recovered solution. High photocatalytic activities were investigated by phenol, 4-chlorophenol and MB degradation under visible light; 40%, 50% and 100% degradation efficiency were achieved, respectively. The 10%V-Ti-700 sample which was composed of 61% anatase and 39% rutile, shows the highest photocatalytic activity and can be reused for at least three times for MB degradation without loss of crystallinity and monomodal mesoporosity. Compared to commercial Degussa P25, all the mesoporous mixed phase samples show better chemical, and physical properties (crystallinity, stability, surface area and porosity), and much higher photocatalytic activity under visible light irradiation.

2.6. References

(1) Antonelli, D. M.; Ying, J. Y. *Angew. Chemie Int. Ed. English* **1995**, *34*, 2014–2017.

(2) Chen, D.; Huang, F.; Cheng, Y.-B.; Caruso, R. A. *Adv. Mater.* **2009**, *21*, 2206–2210.

(3) Park, Y.-C.; Chang, Y.-J.; Kum, B.-G.; Kong, E.-H.; Son, J. Y.; Kwon, Y. S.; Park, T.; Jang, H. M. *J. Mater. Chem.* **2011**, *21*, 9582–9586.

(4) Yoshitake, H.; Sugihara, T.; Tatsumi, T. *Chem. Mater.* **2002**, *14*, 1023–1029.

(5) Wang, D.; Choi, D.; Yang, Z.; Viswanathan, V. V.; Nie, Z.; Wang, C.; Song, Y.; Zhang, J.-G.; Liu, J. *Chem. Mater.* **2008**, *20*, 3435–3442.

(6) Ortel, E.; Sokolov, S.; Zielke, C.; Lauermann, I.; Selve, S.; Weh, K.; Paul, B.; Polte, J.; Kraehnert, R. *Chem. Mater.* **2012**, *24*, 3828–3838.

(7) Armelao, L.; Barreca, D.; Bottaro, G.; Gasparotto, A.; Tondello, E.; Ferroni, M.; Polizzi, S. *Chem. Mater.* **2004**, *16*, 3331–3338.

(8) Lee, J.; Orilall, M. C.; Warren, S. C.; Kamperman, M.; DiSalvo, F. J.; Wiesner, U. *Nat. Mater.* **2008**, *7*, 222–228.

(9) Pan, J. H.; Lee, W. I. *Chem. Mater.* **2006**, *18*, 847–853.

(10) Feng, N.; Wang, Q.; Zheng, A.; Zhang, Z.; Fan, J.; Liu, S.-B.; Amoureux, J.-P.; Deng, F. *J. Am. Chem. Soc.* **2013**, *135*, 1607–1616.

(11) Wu, Z.; Dong, F.; Liu, Y.; Wang, H. *Catal. Commun.* **2009**, *11*, 82–86.

(12) Yang, X.; Ma, F.; Li, K.; Guo, Y.; Hu, J.; Li, W.; Huo, M.; Guo, Y. *J. Hazard. Mater.* **2010**, *175*, 429–438.

(13) Hanaor, D. A. H.; Sorrell, C. C. *J. Mater. Sci.* **2010**, *46*, 855–874.

(14) Zhang, J.; Xu, Q.; Feng, Z.; Li, M.; Li, C. *Angew. Chem. Int. Ed. Engl.* **2008**, *47*, 1766–1769.

(15) Lee, G. H.; Zuo, J.-M. *J. Am. Ceram. Soc.* **2004**, *87*, 473–479.

(16) Yin, S.; Yamaki, H.; Komatsu, M.; Zhang, Q.; Wang, J.; Tang, Q.; Saito, F.; Sato, T. *J. Mater. Chem.* **2003**, *13*, 2996.

(17) Bucharsky, E. C.; Schell, G.; Oberacker, R.; Hoffmann, M. J. *J. Eur. Ceram. Soc.* **2009**, *29*, 1955–1961.

(18) Wijnhoven, J. E. *Science (80-.).* **1998**, *281*, 802–804.

(19) Francisco, M. S. P.; Mastelaro, V. R. *Chem. Mater.* **2002**, *14*, 2514–2518.

(20) Storck, S.; Bretinger, H.; Maier, W. F. *Appl. Catal. A Gen.* **1998**, *174*, 137–146.

(21) Kjellman, T.; Asahina, S.; Schmitt, J.; Impéror-Clerc, M.; Terasaki, O.; Alfredsson, V. *Chem. Mater.* **2013**, *25*, 4105–4112.

(22) Mandal, M.; Kruk, M. *Chem. Mater.* **2012**, *24*, 149–154.

(23) Naldoni, A.; Allieta, M.; Santangelo, S.; Marelli, M.; Fabbri, F.; Cappelli, S.; Bianchi, C. L.; Psaro, R.; Dal Santo, V. *J. Am. Chem. Soc.* **2012**, *134*, 7600–7603.

(24) Bhattacharyya, K.; Varma, S.; Tripathi, A. K.; Bharadwaj, S. R.; Tyagi, A. K. *J. Phys. Chem. C* **2008**, *112*, 19102–19112.

(25) Bulánek, R.; Čapek, L.; Setnička, M.; Čičmanec, P. *J. Phys. Chem. C* **2011**, *115*, 12430–12438.

(26) Hasegawa, G.; Sato, T.; Kanamori, K.; Nakano, K.; Yajima, T.; Kobayashi, Y.; Kageyama, H.; Abe, T.; Nakanishi, K. *Chem. Mater.* **2013**, *25*, 3504–3512.

(27) Reddy, B. M.; Ganesh, I.; Reddy, E. P. *J. Phys. Chem. B* **1997**, *101*, 1769–1774.

(28) Kwon, D. W.; Park, K. H.; Hong, S. C. *Appl. Catal. A Gen.* **2013**, *451*, 227–235.

(29) Sun, M.; Li, D.; Chen, Y.; Chen, W.; Li, W.; He, Y.; Fu, X. *J. Phys. Chem. C* **2009**, *113*, 13825–13831.

(30) Nordlinder, S.; Augustsson, A.; Schmitt, T.; Guo, J.; Duda, L. C.; Nordgren, J.; Gustafsson, T.; Edström, K. *Chem. Mater.* **2003**, *15*, 3227–3232.

(31) Ali, A.; Ruzybayev, I.; Yassitepe, E.; Shah, S. I.; Bhatti, A. S. *J. Phys. Chem. C* **2013**, *117*, 19517–19524.

(32) Zhang, Y.-H.; Reller, A. *Mater. Sci. Eng. C* **2002**, *19*, 323–326.

(33) Shannon, R. D. *Acta Crystallogr. Sect. A* **1976**, *32*, 751–767.

(34) Liu, H.; Wu, Y.; Zhang, J. *ACS Appl. Mater. Interfaces* **2011**, *3*, 1757–1764.

(35) Trifirò, F. *Catal. Today* **1998**, *41*, 21–35.

(36) Rodríguez-Talavera, R.; Vargas, S.; Arroyo-Murillo, R.; Montiel-Campos, R.; Haro-Poniatowski, E. *J. Mater. Res.* **2011**, *12*, 439–443.

(37) Kumar, K.-N. P.; Fray, D. J.; Nair, J.; Mizukami, F.; Okubo, T. *Scr. Mater.* **2007**, *57*, 771–774.

(38) Zhang, H. D.; Shen, Y.; Zheng, X. X. In *Advanced Materials Research*; 2011; Vol. 239-242, pp. 2002–2005.

(39) Gurulakshmi, M.; Selvaraj, M.; Selvamani, A.; Vijayan, P.; Sasi Rekha, N. R.; Shanthi, K. *Appl. Catal. A Gen.* **2012**, *449*, 31–46.

(40) YANG, X.; CAO, C.; HOHN, K.; ERICKSON, L.; MAGHIRANG, R.; HAMAL, D.; KLABUNDE, K. *J. Catal.* **2007**, *252*, 296–302.

(41) Herrmann, J.-M.; Disdier, J.; Deo, G.; Wachs, I. E. *J. Chem. Soc. Faraday Trans.* **1997**, *93*, 1655–1660.

(42) Hegazy, A.; Prouzet, E. *Chem. Mater.* **2012**, *24*, 245–254.

(43) Kho, Y. K.; Iwase, A.; Teoh, W. Y.; Mädler, L.; Kudo, A.; Amal, R. *J. Phys. Chem. C* **2010**, *114*, 2821–2829.

(44) Hurum, D. C.; Agrios, A. G.; Gray, K. A.; Rajh, T.; Thurnauer, M. C. *J. Phys. Chem. B* **2003**, *107*, 4545–4549.

(45) Scanlon, D. O.; Dunnill, C. W.; Buckeridge, J.; Shevlin, S. A.; Logsdail, A. J.; Woodley, S. M.; Catlow, C. R. A.; Powell, M. J.; Palgrave, R. G.; Parkin, I. P.; Watson, G. W.; Keal, T. W.; Sherwood, P.; Walsh, A.; Sokol, A. A. *Nat. Mater.* **2013**, *12*, 798–801.

(46) Deák, P.; Aradi, B.; Frauenheim, T. *J. Phys. Chem. C* **2011**, *115*, 3443–3446.

(47) Lu, W.; Gao, S.; Wang, J. *J. Phys. Chem. C* **2008**, *112*, 16792–16800.

(48) Chang, Y.; Xu, J.; Zhang, Y.; Ma, S.; Xin, L.; Zhu, L.; Xu, C. *J. Phys. Chem. C* **2009**, *113*, 18761–18767.

(49) Hussain, M.; Bensaid, S.; Geobaldo, F.; Saracco, G.; Russo, N. *Ind. Eng. Chem. Res.* **2011**, *50*, 2536–2543.

(50) Conte, P.; Loddo, V.; De Pasquale, C.; Marsala, V.; Alonzo, G.; Palmisano, L. *J. Phys. Chem. C* **2013**, *117*, 5269–5273.

(51) Carneiro, J. T.; Savenije, T. J.; Moulijn, J. A.; Mul, G. *J. Phys. Chem. C* **2010**, *114*, 327–332.

CHAPTER 3. MESOPOROUS, BLUE MoO_{3-x} MATERIAL AS EFFICIENT ELECTROCATALYST FOR HYDROGEN EVOLUTION REACTION

3.1 Introduction

Pt and Pt based materials are known as the most efficient electrocatalysts for HER in both acidic and alkaline conditions. However, the scarcity and high cost of Pt do not allow widespread use as electrocatalysts for HER. The development of electrocatalysts that are Pt free, highly active and operable in both acidic and alkaline conditions, remains a challenging task. In recent years, metal sulfides (MoS_2, FeS_2 et al.),[1,2] carbon based (carbon nanotubes, graphitic carbon et al.)[3] or hybrid materials (carbon supported metal oxide, reduced graphene oxide supported metal sulfides et al.)[4,5] have been intensively studied as replacements for Pt based electrocatalysts. These materials have been reported that have high active HER activity and stability in acidic media or alkaline media. Nevertheless, electrocatalysts that could drive HER in both acidic and alkaline systems were rarely reported.

Molybdenum based materials (such as molybdenum carbonitride (MoCN), molybdenum diselenide ($MoSe_2$), bimetallic Ni-Mo-C materials) have been investigated as active HER electrocatalysts.[6] Molybdenum disulfides (MoS_2) are Mo based materials that have been widely studied and have exhibited promising HER activity.[7] In 2005, Hinnemann et al. first reported that the under-coordinated sulfur atoms at the edges of

MoS_2 have very similar properties to natural HER active enzymatic centers.[8] Since then, MoS_2 materials have been extensively investigated for HER. However, its catalytic HER activity is limited by the number of active sites.

Molybdenum oxide (MoO_3) is a low cost, nontoxic and environmentally benign transition metal with high stability. MoO_3 is widely employed in heterogeneous catalysis, electrocatalysis, and also in capacitors, lithium-ion battery applications.[9] MoO_3 has two major phases, the metastable monoclinic phase (β-MoO_3) and thermodynamically stable orthorhombic phase (α-MoO_3) (crystal structures illustrated in Figure 3.1). The orthorhombic phase has a layered structure which is formed by stacking bilayer sheets of MoO_6 octahedra with van der Waals forces.[10] This structure is suitable for insertion/removal of small ions such as H^+, and therefore is intensively studied as a supercapacitor. However, without active edges like those of MoS_2, intrinsic MoO_3 material had not been reported as an electrocatalyst for HER to the best of our knowledge.

Herein, mesoporous MoO_{3-x} serve as an active HER electrocatalyst in alkaline and acidic conditions were prepared. Without any extrinsic dopants, alloys, or any hybrid metals. The HER activity of MoO_3 has been developed and improved by considering the following aspects. First is the mesoporosity of MoO_3, since the mesoporous structure was shown previously to effectively enhance the activity of various kinds of metal oxides (WO_3, TiO_2, Co_3O_4, etc.) in catalytic reactions.[11]; Second is the design of non-stoichiometric structure MoO_{3-x} with oxygen vacancies; Last is the phase of MoO_3, the orthorhombic α-MoO_3 (thermodynamically stable phase) has a layered structure which is suitable for

insertion/removal of small ions such as H^+ in electrochemical reactions.[12,13] Above all, we are reporting mesoporous MoO_{3-x} material as a highly efficient HER catalyst in both acidic and alkaline conditions.

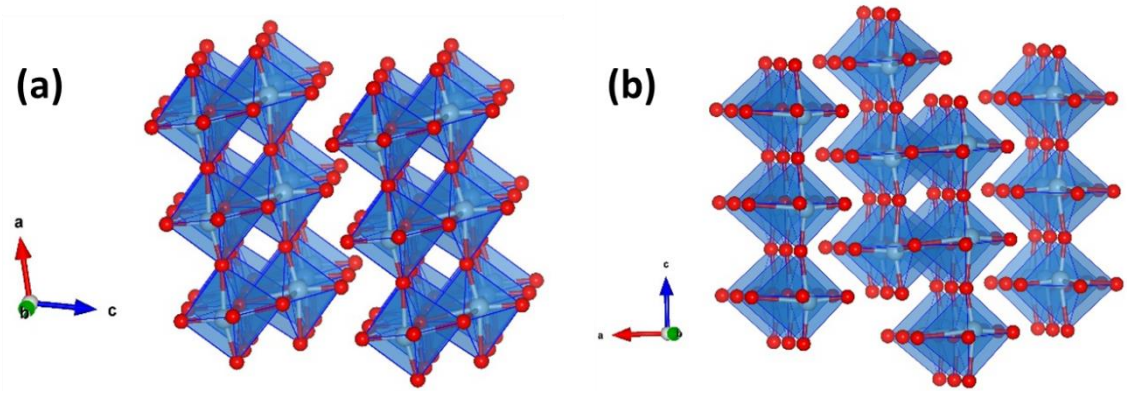

Figure 3. 1 The crystal structure of (a) monoclinic and (b) orthorhombic phase MoO_3.

3.2. Experimental Section

3.2.1. Catalyst preparation

In a typical synthesis, 0.26 g commercial MoO_3 (*com*MoO_3) was dissolved in 3 mL H_2O_2 until a clear yellow gel was obtained. Then 0.1 g PEO-*b*-PS surfactant was dissolved in 7 mL THF solvent and stirred for 30 min. After all the surfactant was dissolved in THF, this solution was dropwise added to the clear yellow gel. After stirring for 30 min, the obtained homogeneous yellow gel was poured into a Petri dish to evaporate THF at ambient conditions. The obtained clear film was collected and calcined at 350 or 450 °C for 3 hrs under air. The blue greyish mesoporous MoO_3 calcined at 350 °C was prepared and labeled as *m*MoO_3. The mesoporous MoO_3 calcined at 450 °C is labeled as *m*MoO_3-450.

3.2.2. Characterization

Powder X-ray diffraction (PXRD) analyses were performed on a Rigaku Ultima IV diffractometer (Cu Kα radiation, λ= 1.5406 A) with an operating voltage of 40 kV and a current of 44 mA. Raman spectra were taken on a Renishaw 2000 Raman microscope with a wavelength of 514 nm, exposure time of 16, and accumulations of 4 times. Nitrogen (N_2) sorption experiments were conducted on a Quantachrome Autosorb-1-1C automated sorption system. Morphological characterization was done using an FEI Nova NanoSEM 450 with an accelerating voltage of 2.0 kV. Transmission electron microscopy (TEM), high resolution transmission electron microscopy (HRTEM), and selected area electron diffraction (SAED) were obtained in a JEOL 2010 UHR FasTEM operating at an accelerating voltage of 200 kV. The samples were prepared by dispersing the material in

methanol. X-ray photoelectron spectroscopy (XPS) measurements were performed in a PHI model 590 spectrometer with multiprobes (ΦPhysical Electronics Industries Inc.), using Al Kα radiation (λ= 1486.6 eV) operated at 250 W. Diffuse reflectance ultraviolet−visible (DR UV−vis) spectra of the powder samples were collected with a diffuse reflectance apparatus attached on a Shimadzu UV-2450 ultraviolet−visible spectrophotometer. GPC measurements were performed using a Waters GPC-1 (1515 HPLC Pump and Waters 717Plus Autoinjector) equipped with a Varian 380-LC evaporative light scattering detector and a Waters 2487 dual absorbance detector, with three Jordi Gel fluorinated DVB columns (1-100 K, 2-10 K and 1-500 Å). Proton nuclear magnetic resonance (1H NMR) spectra were recorded on a Bruker Avance 300 MHz spectrometer.

3.2.3. Electrochemical Studies

The cell setup consisted of a working electrode (Ni foam or carbon foam) coated with the sample, an SCE reference electrode, a graphite rod electrode, and 0.1 M KOH or H_2SO_4 solution as the electrolyte. Linear sweep voltammetry was carried out at 5 mV/s for the polarization curves. All polarization curves were iR-corrected. The working electrode was prepared as follows: 10 mg of active material sample and 10 mg of carbon (VulcanXC-72) were dispersed in a mixture of deionized distilled water (DDW) and isopropanol (4 mL:1 mL) and sonicated for 3 min, followed by adding 20 μL of polytetrafluoroethylene (PTFE) solution (60% in water, Sigma) and sonicating for 5 min to form a suspension. A 20 μL suspension was deposited onto Ni foam or carbon foam using a micropipette. The catalyst

loadings were 0.2 mg/cm^2.

3.3. Results

3.3.1. Physicochemical Properties

Shown in Figure 3.2a, all the diffraction lines of the as-synthesized *m*MoO_3 that can be assigned to the orthorhombic phase (α-MoO_3 phase, JCPDS No. 05-0508), which is crystallized in a layered structure composed of MoO_6 octahedra by sharing edges and corners. The commercial MoO_3 (*com*MoO_3) sample also shows the orthorhombic phase (α-MoO_3 phase, JCPDS No. 35-0609), but with different crystal parameters. No diffraction lines of other phases (β-MoO_3, h-MoO_3) were found in both samples. The *m*MoO_3 shows much lower crystallinity than *com*MoO_3, which may be due to the formation of a mesostructure that breaks the long-term crystallinity. The phase of molybdenum oxide samples can be further characterized by Raman spectroscopy, due to each phase occupying different atomic arrangements with different Raman vibrational bands. The three characteristic vibrational modes of the orthorhombic phase at 289, 818, and 995 cm^{-1} are displayed in both samples.[14] All observed vibrational modes are in agreement with the α-MoO_3 phase reported in the literature.[15]

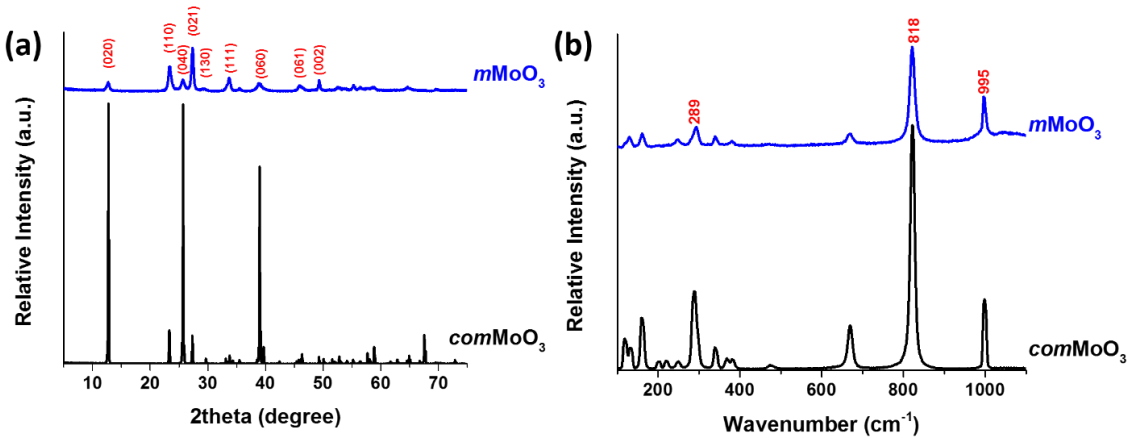

Figure 3. 2 (a) PXRD patterns and (b) Raman spectroscopy for *com*MoO_3 (black pattern) and mesoporous *m*MoO_3 (blue pattern).

Figure 3.3a-c shows field-emission scanning electron microscopy (FESEM) images for the mesoporous molybdenum (*m*MoO_3) sample with various magnification scales. In terms of SEM results, the *m*MoO_3 sample is composed of small particles, which have sizes smaller than 100 nm. The porosity was formed by the aggregation of nanoparticles, and the pores are the connected intraparticle voids. For comparison, the SEM image of *com*MoO_3 sample was also recorded (Figure 3.3d). The commercial sample is composed of giant chunks of crystal (5-10 μm) instead of nanoparticles. No porosity could be observed in this sample.

In a typical TEM image shown in Figure 3.3e, the particle size of *m*MoO_3 is in the range of 50-100 nm, in accordance with SEM results. The *m*MoO_3 has a porous structure. Most of the pores are in the range of mesopores (20-40 nm). In a higher magnification image (Figure 3.3e, onset image), a typical mesopore connected with crystalline particles with a diameter around 30 nm is clearly observed. In Figure 3.3f, the measured *d*-spacing (≈0.35 nm) corresponds to the (040) planes of the α-MoO_3 phase, which is in accordance with XRD and Raman results.

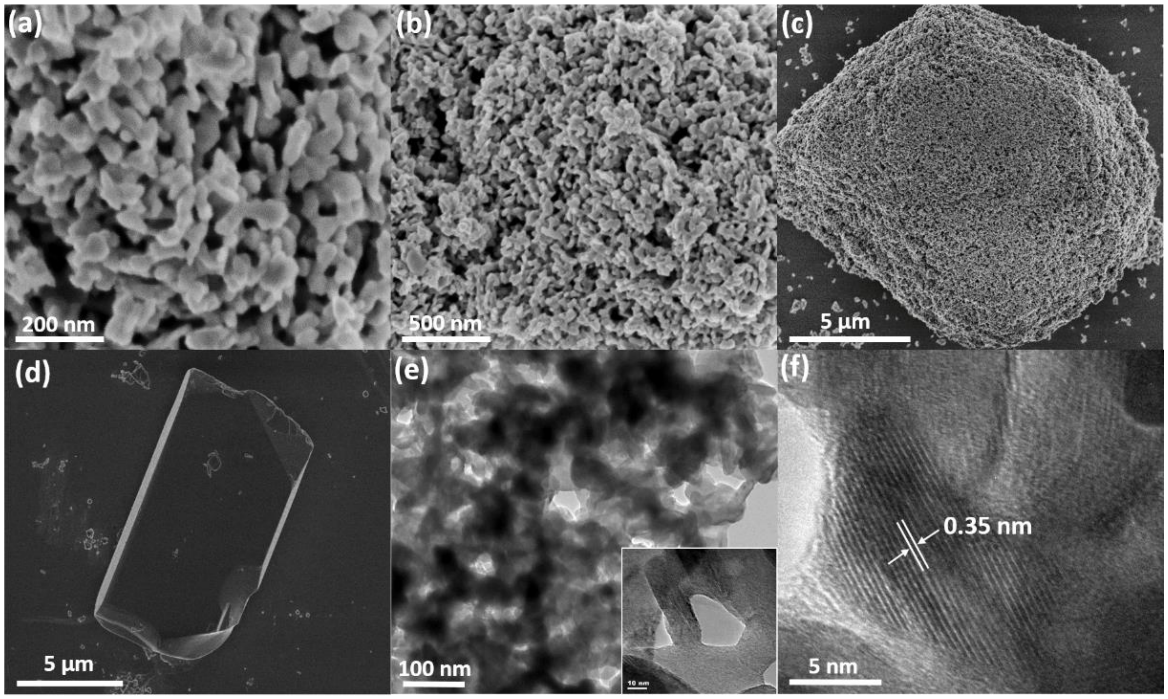

Figure 3. 3 Scanning electron microscopy (SEM) images (a-c) for mesoporous *m*MoO_3 sample with different magnifications. Porosity could be observed with different scales: (a) 200 nm, (b) 500 nm, and (c) 5 µm. (d) The SEM image of *com*MoO_3 as a comparison. (e) The transmission electron microscopy (TEM) image of *m*MoO_3 with well dispersed mesopores (20-40 nm), a typical mesopore is illustrated in the onset image with a scale bar of 10 nm. (f) High resolution TEM of *m*MoO_3, the *d*-spacing (0.35 nm) of (040) plane of α-MoO_3 is displayed.

3.3.2. Oxygen Deficient Structure

Figure 3.4a exhibits the Mo 3d XPS core spectra of the as-prepared *m*MoO_3 and *com*MoO_3. The Mo 3d core level spectrum of the *com*MoO_3 (lower curve) consists of a spin orbit doublet with peaks at 235.6 and 232.4 eV, which are attributed to $3d_{3/2}$ and $3d_{5/2}$ of the Mo cations in high oxidation states (Mo^{6+}). However, for the *m*MoO_3 sample, an obvious shift to the lower binding energy can be observed. Without changing the energy difference (Δ = 3.2 eV) between two peaks, Mo $3d_{3/2}$ shifted to 234.4 eV and Mo $3d_{5/2}$ shifted to 231.2 eV. Both of these two peaks can be assigned to Mo^{5+} species.[16] The presence of Mo^{5+} cations leads to an increment in electron density and a weaker binding effect. Figure 3.4b shows the O 1s spectra, for the *com*MoO_3 material (lower curve), no obvious shift is observed. All peak positions are in good accord with literature values. The main component peak at 531.3 eV (blue curve) corresponds to the lattice oxygen (O^{2-});[17] the other two component peaks (533.1 and 534.6 eV) are attributed to surface adsorbed species (OH^-, O^- et al.).[18,19] On the contrary, the major O 1s peak of *m*MoO_3 shifted to a much lower energy (529 eV), which indicates a change in the coordination configuration of Mo with O. As reported, the O 1s shifts to a lower energy level in line with the transfer of electrons to the neighboring oxygen vacancies.[20] The presence of oxygen vacancies is suggested. Binding energy shifts to lower energy levels was also reported in other oxygen-deficient TMOs, such as the most widely studied material: TiO_{2-x}.[21]

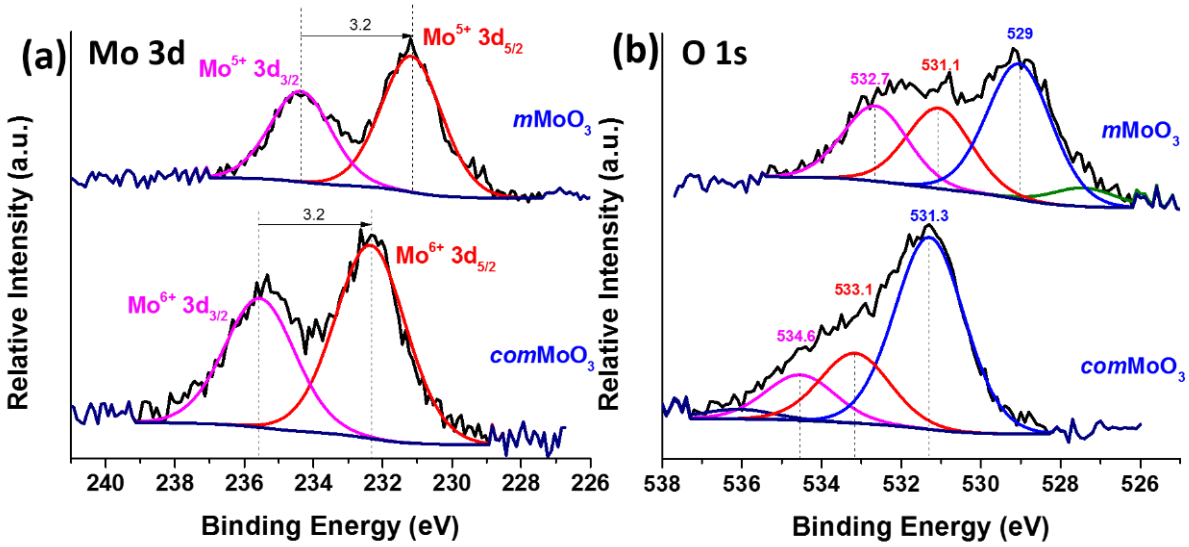

Figure 3. 4 XPS spectra details for (a) Mo 3d binding energy regions, and (b) O1s level. Lower and upper curves are *com*MoO_3 and as-synthesized *m*MoO_3, respectively.

The *com*MoO_3 possesses a light greenish color, while the as-synthesized *m*MoO_3 has a blue color. Similar to the case with oxygen-deficient WO_{3-x} and TiO_{2-x}, the blue color of the transition metal oxide originates from the characteristic outer *d*-shell electrons.[22] To study the optical properties of molybdenum oxides, diffuse reflectance ultraviolet−visible (DR UV−vis) spectra was applied. In Figure 3.5a, the *com*MoO_3 (black curve) shows a major absorption band in the UV range (< 410 nm) and a cut-off wavelength at 420 nm. The *m*MoO_3 shows a new and broad absorption band in the visible range (> 410 nm), which means a much smaller band gap than *com*MoO_3. Since there are no extrinsic dopants in the *m*MoO_3 system, the narrowing of band gap could be ascribed to the presence of oxygen vacancies.

The existence of oxygen vacancies was further investigated by oxygen temperature-programmed oxidation (TPO). The O_2 TPO profiles of *m*MoO_3 and *com*MoO_3 are compiled in Figure 3.5b. The O_2 TPO profile of *com*MoO_3 (black curve) exhibits no obvious oxygen consumption peaks, indicating no oxygen vacancies on the surface of *com*MoO_3. While the O_2 TPO profile of *m*MoO_3 shows a predominant oxygen consumption peak around 460 °C, suggesting the existence of oxygen vacancies in the *m*MoO_3 sample, which are able to react with flowing oxygen. Both samples after O_2 TPO treatment were collected (onset images in Figure 3.5b). A significant color change of *m*MoO_3 could be observed. The *m*MoO_3 lost its original blue color, due to oxygen vacancies that were filled by the oxygen flow.

Figure 3.5c shows that with oxygen vacancies in different sites (V1, V2, and V3), a much smaller band gap could be obtained compared to MoO_3 without any oxygen

vacancies. The smaller band gap observation is in agreement with the results from DR UV-vis spectroscopy. The α-MoO_3 has a layered structure with three different sites of oxygen that can form vacancies, as shown in Figure 3.5d. A vacancy at site 1 is most thermodynamically stable.

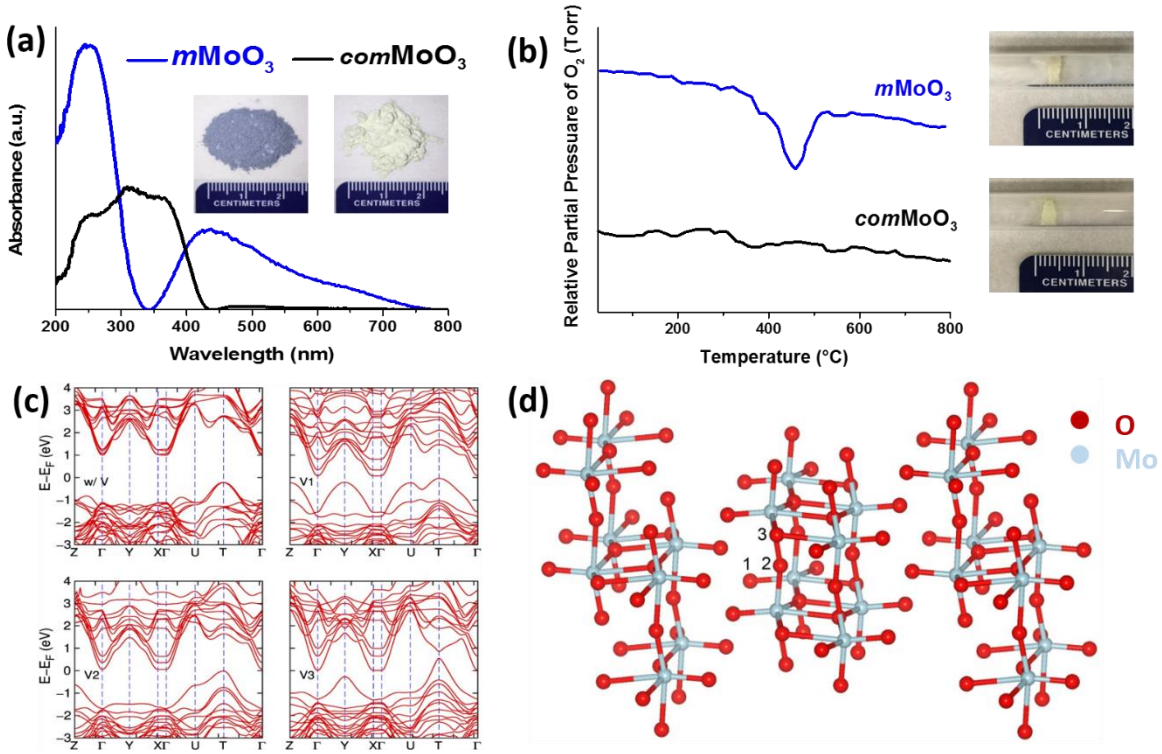

Figure 3. 5 (a) DR UV-vis spectra and photos (onset images) for *com*MoO_3 and as-synthesized *m*MoO_3. (b) Oxygen temperature-programmed oxidation (TPO) for *com*MoO_3 and *m*MoO_3 samples. The onset images display the color change of samples after TPO treatment. (c) Electronic band structure of orthorhombic MoO_3 without (w/ V) and with (V1, V2, and V3) vacancies at different sites. (d) Optimized structure of MoO_3 in which Mo and O atoms are shown in cyan and red colors. Numbers (1, 2, and 3) indicate three different positions of O which are considered for vacancies.

3.3.3 Hydrogen Evolution Reaction

The electrocatalytic activities of the as-synthesized *m*MoO_3 materials were examined in both alkaline (0.1 M KOH) and acidic aqueous (0.1 M H_2SO_4) solutions. Figure 3.5a shows the HER polarization curves of various electrocatalyts in 0.1 M KOH solution. Bare Ni foam (black curve) requires a large overpotential (~225 mV) to achieve a 10 mA/cm^2 HER current density. The *com*MoO_3, which was loaded on Ni foam, performed similarly as bare Ni foam (red curve). No improvement can be observed for the HER activity. As an extended study, the *m*MoO_3 material calcined at higher temperature (450 °C, labeled as *m*MoO_3-450) was also tested by HER, in order to have a rough idea about whether the calcination temperature affects catalytic properties. For *m*MoO_3 and *m*MoO_3-450 samples, the current densities reach 10 mA/cm^2 at potentials of 122 mV and 153 mV, respectively. These overpotential values are much closer to the Pt/C catalyst system (η = 65 mV for j = -10 mV/cm^2) as compared to bare Ni or commercial sample tested under identical conditions, indicating excellent catalytic activity in mesoporous samples, especially for the *m*MoO_3 sample.

Besides activity, stability is another major concern for all electrocatalysts. The electrochemical stability of mMoO_3 was evaluated by monitoring the current density during continuous operation at -0.174 V (vs. RHE) under alkaline conditions. The current density versus time data provided in Figure 3.5b show that the value remains stable after a slight initial increase in the beginning several hours. The current density does not vary significantly in 11 h, manifesting excellent stability of mesoporous MoO_3 during the

electrochemical experiments. Hydrogen evolution can be directly observed in the onset image of Figure 3.6b.

Due to the reported poor corrosion stability of Mo materials in acidic media, few studies in acidic media were reported. The HER activity of all prepared catalysts was further tested under acidic condition (0.1 M H_2SO_4). Shown in Figure 3.6c, similar to alkaline conditions (0.1 M KOH), bare Ni foam exhibits the lowest activity (η = 510 mV for j = -10 mV/cm^2). With the deposition of *com*MoO_3 on Ni foam, no enhanced HER activity can be observed. However, to achieve -10 mV/cm^2 current density, *m*MoO_3 samples show higher activity, which is closer to the best HER electrocatalyst Pt/C (~63 mV) under identical conditions.

To further confirm the HER performance of *m*MoO_3 material, one more concern is that Ni foam used as a working electrode may also contribute to HER activity. This foam is low cost and conductive metal which qualifies as a working electrode.[23] The HER activity of Ni foam itself is comparable to some traditional metallic catalysts, due to the low resistance of Ni and large surface area of the foam.[24,25] There are several studies that report nickel and nickel-molybdenum electrocatalysts for hydrogen evolution.[26,27] In order to investigate if there is a synergistic effect between Ni and Mo, different working electrodes (carbon foams) were studied. The *com*MoO_3 and mesoporous MoO_3 samples were deposited on carbon foam (C foam) with the same amounts (0.2 mg/cm^2) as on the Ni foam. Figure 3.6d shows the HER activity results in 0.1 M KOH media, with carbon foam applied as a working electrode. As-prepared *m*MoO_3 samples (*m*MoO_3, *m*MoO_3-450)

exhibit much higher HER activity than bare C foam or the c*om*MoO_3 sample. Overpotentials of 0.35 and 0.38 V can lead to current densities of 20 mA/cm^2 for *m*MoO_3 and *m*MoO_3-450, respectively. For comparison, the bare C foam without any catalyst deposition under identical experimental conditions exhibits very low HER catalytic activity. With the deposition of *com*MoO_3 sample on C foam, no significant improvement of HER catalytic activity can be observed. Above all, without the support of Ni foam, *m*MoO_3 still shows much higher activity than *com*MoO_3, indicating the Ni foam is not a key factor for the high HER activity in this study.

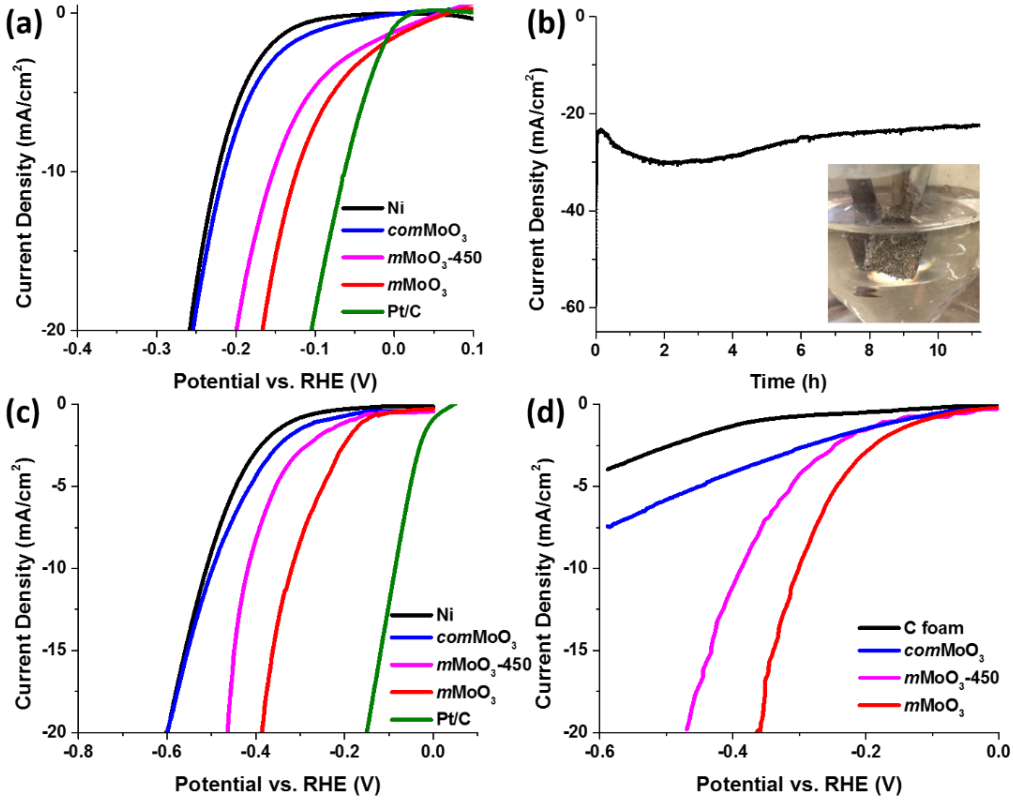

Figure 3. 6 (a) Polarization curves of *m*MoO_3 materials on Ni foam electrode in 0.1 M KOH, along with bare Ni foam, *com*MoO_3 and Pt/C for comparison. (b) Time dependence of current density during HER over 11 h at fixed overpotential -0.174 V for *m*MoO_3 sample in 0.1 M KOH. Onset image: photo was taken during HER using *m*MoO_3 sample, H_2 bubbles can be clearly observed on the electrode surface. (c) Polarization curves of all materials on Ni foam electrode in 0.1 M H_2SO_4. (d) Polarization curves of *m*MoO_3 materials on carbon foam electrode in 0.1 M KOH, along with bare carbon foam and *com*MoO_3 for comparison.

3.4 Discussion

3.4.1. The Decisive Role of Structure

The mesoporous structure of *m*MoO_3 material possesses a decisive role for improving the charge transfer rate and conductivity. Due to their pore shape, large pore size, high surface area, and high electrical conductivity, mesoporous metal oxides have shown superior performances for electrochemical applications.[28,29] The mesopores, which make it easy to effectively transport guest molecules/ions to the active sites located in internal particle, significantly enhance the charge transfer process during electrochemical reactions. In this study, in both alkaline and acidic medias, the mesostructure contributes to the HER activity in two aspects. First of all, the mesopores with high surface area provide more active sites for HER. The *m*MoO_3 (52 m^2/g) possesses a much higher surface area than *com*MoO_3 (2 m^2/g) by Brunauer-Emmett-Teller (BET) measurements. Generally, higher surface area comes with more active sites;[30] Second, mesopores facilitate the mass transport of fluids and the contact of reactant molecules/ions with active sites.[31,32] In *com*MoO_3 system, without a porous structure, electrolyte is only able to contact the surface of the bulk material, leading to the possible accumulation of electrons/ions/molecules on the surface and further decreases the reaction efficiency. In contrast, in the *m*MoO_3 system, mesopores act as open access to introduce fluids to contact with the internal structure, which effectively improves the mass transport without blocking active sites.[33] Thus, the conductivity should be effectively promoted by the mesostructure.

In order to prove the mesostructure is able to improve conductivity, we further

conducted electrochemical impedance studies under HER reaction conditions by using Electrochemical Impedance Spectroscopy (EIS), shown in Figure 3.7a. The high-frequency intersection with the *x*-axis represents the uncompensated solution resistance (R_s, ohmic resistance), which is comparable for all catalysts. The apparent lower Faradaic resistance in the electrochemical impedance spectrum, is related to a higher charge-transfer rate in HER. The EIS spectra for the bare Ni foam and the *com*MoO_3 exhibit high charge transfer resistance values (R_{ct}= 90 and 66 Ω, respectively). The R_{ct} of *m*MoO_3 is 43 Ω in 0.1 M KOH, indicating a better conductivity and an enhanced electrocatalytic performance. The R_{ct} values follows the order *m*MoO_3 < *com*MoO_3< bare Ni foam, in correlation with an inverse HER activity, suggesting the charge transfer process is a vital factor in this HER study. Mesopores significantly facilitate the charge transfer.

Another property that may affect the HER activity is the oxygen-deficient structure. Structural defects are always considered as active sites in catalytic reactions. Similar to HER, defects such as oxygen vacancies were regarded as active sites.[34,4] The presence of oxygen vacancies enhances the interaction between oxygen-containing species and metal oxide surfaces.[35] In this study, oxygen vacancies may favor the adsorption of water molecules (or H_3O^+), which serve as electron acceptors, then lower the HER energy barrier. In terms of DFT calculations (Figure 3.5c), the introduction of oxygen vacancies in MoO_3 gives rise to electrical conductivity. By reducing the metal cations, MoO_3 can be made to be semi-metallic due to filling of the *d*-band.[36]

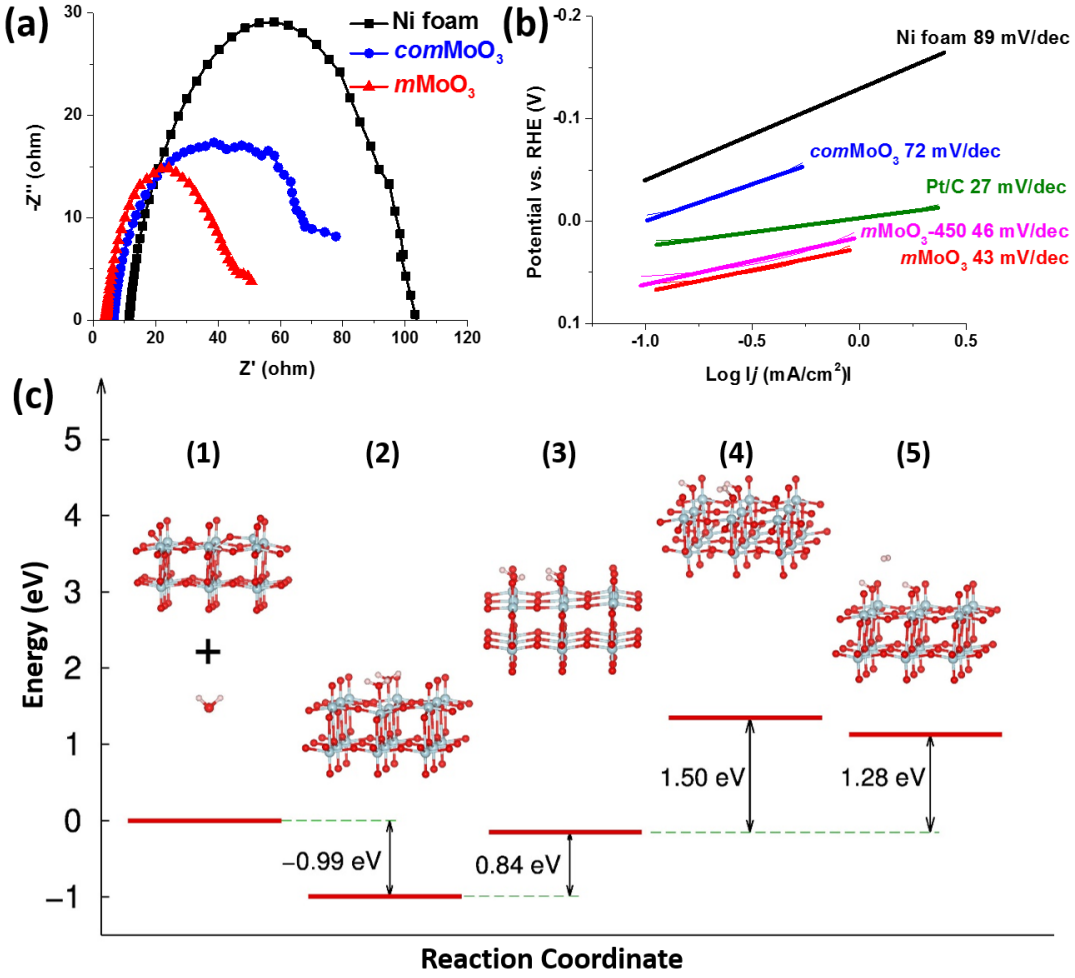

Figure 3. 7 (a) Nyquist plots obtained from EIS measurements in 0.1 M KOH solution on the Ni foam electrode at an anodic polarization potential of (-0.09V vs RHE). (b) Corresponding Tafel plots of *m*MoO_3 samples in 0.1 M KOH, along with bare Ni foam, *com*MoO_3 and Pt/C for comparison. (c) Proposed reaction pathway and the energy barrier profiles of *m*MoO_3 sample.

3.4.2. Mechanism Studies

There are different mechanisms for HER in different conditions. The direct difference between alkaline and acidic mechanisms is the nature of the proton source [H_2O or H_3O^+(see equations below)].[37,38]

The HER in an alkaline media:

Volmer-Heyrovsky: $H_2O_{(l)} + e^- \leftrightarrow H_{ads} + OH^-$

$H_{ads} + H_2O_{(l)} + e^- \leftrightarrow H_{2\,(g)} + OH^-$

Volmer-Tafel: $H_2O_{(l)} + e^- \leftrightarrow H_{ads} + OH^-$

$H_{ads} + H_{ads} \leftrightarrow H_{2\,(g)}$

The HER in an acidic media:

Volmer-Heyrovsky: $H_3O^+ + e^- \leftrightarrow H_{ads} + H_2O_{(l)}$

$H_{ads} + H_3O^+ + e^- \leftrightarrow H_{2\,(g)} + H_2O$

Volmer-Tafel: $H_3O^+ + e^- \leftrightarrow H_{ads} + H_2O_{(l)}$

$H_{ads} + H_{ads} \leftrightarrow H_{2\,(g)}$

After hydrogen atoms adsorbed on the surface of the catalyst, subsequent production of H_2 may occur via two different pathways. Either via the Volmer-Heyrovsky mechanism (ion + atom reaction), the adsorbed hydrogen atom (H_{ads}) accepts an electron and then combines with another proton source (H_2O or H_3O^+) to release H_2; or via the direct combination of two H_{ads}, which is called the Volmer-Tafel mechanism (combination reaction).[39]

To determine the predominant HER mechanism, the Tafel slope is a useful indicator

by suggesting the additional voltage needed to increase the current density by 10-fold. Generally, the smaller the value, the faster the HER rate. In **Figure 3.7b**, under alkaline conditions, the measured Tafel slope of Pt/C is 27 mV/dec, indicating a fast Volmer-Tafel process. For *m*MoO_3 and *m*MoO_3-450 samples, Tafel slopes of 43 and 46 mV/dec are observed, suggesting a fast HER rate via the Volmer-Heyrovsky process. With Tafel slope close (or larger) to 116 mV/dec, the HER rate can be defined as a slow discharge reaction via the Volmer-Heyrovsky process, such as for Tafel slopes of bare Ni and *com*MoO_3 materials.[40] Another observation is the earlier onset of overpotential of *m*MoO_3 materials than Pt/C material, which suggests hydrogen adsorption close to equilibrium.[41,42]

The HER pathway of *m*MoO_3 was then schematically described in Figure 3.7c based on DFT calculations. Because α-MoO_3 has a layered structure and the site 1 oxygen vacancy (Figure 3.5d) on the top of a layer is preferred for an oxygen vacancy to form, we then constructed a MoO_3 slab based on these layers with the vacancy at this site. In alkaline solution, the reaction pathway mainly involved H_2O (proton source) adsorption (transition state 2, Figure 3.7c), reduction on the *m*MoO_3 surface to form hydrogen atom adsorbed on the active site (transition state 3), followed by H_2 formation (transition state 4) and desorption (transition state 5). Through DFT calculations, the oxygen vacancies close to Mo^{5+} were found to be the HER active sites. The initial state (1) in Figure 3.6c is the *m*MoO_3 with oxygen vacancies, surrounded by H_2O molecules in the electrolyte. The energy barrier for transition state (2), H_2O molecules adsorbed on the *m*MoO_3 surface is found to be 0.99 eV. The presence of oxygen vacancies significantly lowered the energy

barrier for H_2O adsorption. The transition state (3) is the reduction of adsorbed H_2O molecules (H_2O_{ads}) and the formation of adsorbed hydrogen atoms (H_{ads}). Since the *m*MoO_3 material followed the Volmer-Heyrovsky mechanism in terms of the experimental Tafel value (43 mV/dec), the H_{ads} would combine with another adjacent H_2O_{ads}. The last step (transition state 5) is the release of the formed H_2 molecule. The H_2 evolution energy barrier of *m*MoO_3 material with oxygen vacancies is much smaller compared to MoO_3 material without oxygen vacancies. Overall, the *m*MoO_3 catalyst possesses suitable adsorption and desorption energy for H_2 evolution. The presence of oxygen vacancies could lower the kinetic energy barrier by facilitating H_2O adsorption and promoting H-H bond formation on two adjacent adsorbed H_{ads} and H_2O_{ads} species.

3.5. Conclusions

In summary, a new mesoporous, crystalline MoO_{3-x} material has been successfully synthesized and identified as a highly active electrocatalyst for HER through experimental and theoretical (DFT) studies. Through a novel, cost effective, and flexible method of dissolving cheap molybdenum in H_2O_2 as precursor, combined with a PEO-*b*-PS template, the as-synthesized material has unique properties of mesoporosity and oxygen-deficiency. The as-synthesized *m*MoO_3 has a much larger surface area (52 m^2/g) than *com*MoO_3 (2 m^2/g), and shows outstanding performance in HER in both acidic and alkaline solution, without the assistance of carbon materials, extrinsic dopants, or other metal alloys. The calculated Tafel slope is as low as 43 mV/dec in 0.1 M KOH and the high activity can be

maintained for more than 11 h. Compared to *com*MoO_3 (66 Ω), the as-synthesized *m*MoO_3 has a much smaller charge transfer resistance (42 Ω). The key factors are mesopores (20-40 nm) that facilitate the charge transfer, and the oxygen vacancies that narrow the bandgap leading to better conductivity. The oxygen vacancies that close to Mo^{5+} are regarded as active sites for HER. All experimental and theoretical data suggest the HER performance highly depends on the unique structure of *m*MoO_3 materials. This study described a novel route to easily synthesize cheap, functional TMO materials with excellent HER activity and sheds light on the search for promising electrocatalysts for practical applications.

3.6. References

(1) Wang, D.-Y.; Gong, M.; Chou, H.-L.; Pan, C.-J.; Chen, H.-A.; Wu, Y.; Lin, M.-C.; Guan, M.; Yang, J.; Chen, C.-W.; Wang, Y.-L.; Hwang, B.-J.; Chen, C.-C.; Dai, H. *J. Am. Chem. Soc.* **2015**, *137*, 1587–1592.

(2) Xu, S.; Li, D.; Wu, P. *Adv. Funct. Mater.* **2015**, *25*, 1127–1136.

(3) Shalom, M.; Gimenez, S.; Schipper, F.; Herraiz-Cardona, I.; Bisquert, J.; Antonietti, M. *Angew. Chemie* **2014**, *126*, 3728–3732.

(4) Wu, R.; Zhang, J.; Shi, Y.; Liu, D.; Zhang, B. *J. Am. Chem. Soc.* **2015**, *137*, 6983–6986.

(5) Kong, D.; Wang, H.; Lu, Z.; Cui, Y. *J. Am. Chem. Soc.* **2014**, *136*, 4897–4900.

(6) Zhao, Y.; Kamiya, K.; Hashimoto, K.; Nakanishi, S. *J. Am. Chem. Soc.* **2015**, *137*, 110–113.

(7) Chen, Z.; Cummins, D.; Reinecke, B. N.; Clark, E.; Sunkara, M. K.; Jaramillo, T. F. *Nano Lett.* **2011**, *11*, 4168–4175.

(8) Hinnemann, B.; Moses, P. G.; Bonde, J.; Jørgensen, K. P.; Nielsen, J. H.; Horch, S.; Chorkendorff, I.; Nørskov, J. K. *J. Am. Chem. Soc.* **2005**, *127*, 5308–5309.

(9) Brezesinski, T.; Wang, J.; Tolbert, S. H.; Dunn, B. *Nat. Mater.* **2010**, *9*, 146–151.

(10) Mai, L. Q.; Hu, B.; Chen, W.; Qi, Y. Y.; Lao, C. S.; Yang, R. S.; Dai, Y.; Wang, Z. L. *Adv. Mater.* **2007**, *19*, 3712–3716.

(11) Liu, B.; Kuo, C.-H.; Chen, J.; Luo, Z.; Thanneeru, S.; Li, W.; Song, W.; Biswas, S.; Suib, S. L.; He, J. *Angew. Chemie* **2015**, *127*, 9189–9193.

(12) Tanisaki, S. *J. Phys. Soc. Japan* **1960**, *15*, 573–581.

(13) Machiels, C. J.; Cheng, W. H.; Chowdhry, U.; Farneth, W. E.; Hong, F.; Mc Carron, E. M.; Sleight, A. W. *Appl. Catal.* **1986**, *25*, 249–256.

(14) Dieterle, M.; Mestl, G. *Phys. Chem. Chem. Phys.* **2002**, *4*, 822–826.

(15) Liang, R.; Cao, H.; Qian, D. *Chem. Commun.* **2011**, *47*, 10305–10307.

(16) Vasilopoulou, M.; Douvas, A. M.; Georgiadou, D. G.; Palilis, L. C.; Kennou, S.; Sygellou, L.; Soultati, A.; Kostis, I.; Papadimitropoulos, G.; Davazoglou, D.; Argitis, P. *J. Am. Chem. Soc.* **2012**, *134*, 16178–16187.

(17) Scanlon, D. O.; Watson, G. W.; Payne, D. J.; Atkinson, G. R.; Egdell, R. G.; Law, D. S. L. *J. Phys. Chem. C* **2010**, *114*, 4636–4645.

(18) Luo, Z.; Poyraz, A. S.; Kuo, C.-H.; Miao, R.; Meng, Y.; Chen, S.-Y.; Jiang, T.; Wenos, C.; Suib, S. L. *Chem. Mater.* **2015**, *27*, 6–17.

(19) Światowska-Mrowiecka, J.; de Diesbach, S.; Maurice, V.; Zanna, S.; Klein, L.; Briand, E.; Vickridge, I.; Marcus, P. *J. Phys. Chem. C* **2008**, *112*, 11050–11058.

(20) Kang, Q.; Cao, J.; Zhang, Y.; Liu, L.; Xu, H.; Ye, J. *J. Mater. Chem. A* **2013**, *1*, 5766–5774.

(21) Chen, H.; Wei, Z.; Yan, K.; Bai, Y.; Yang, S. *J. Phys. Chem. Lett.* **2014**, *5*, 2890–2896.

(22) Gordon, T. R.; Cargnello, M.; Paik, T.; Mangolini, F.; Weber, R. T.; Fornasiero, P.; Murray, C. B. *J. Am. Chem. Soc.* **2012**, *134*, 6751–6761.

(23) Chinthaginjala, J. K.; Lefferts, L. *Carbon N. Y.* **2009**, *47*, 3175–3183.

(24) Chang, Y.-H.; Lin, C.-T.; Chen, T.-Y.; Hsu, C.-L.; Lee, Y.-H.; Zhang, W.; Wei, K.-H.; Li, L.-J. *Adv. Mater.* **2013**, *25*, 756–760.

(25) Ledendecker, M.; Clavel, G.; Antonietti, M.; Shalom, M. *Adv. Funct. Mater.* **2015**, *25*, 393–399.

(26) Chen, W.-F.; Sasaki, K.; Ma, C.; Frenkel, A. I.; Marinkovic, N.; Muckerman, J. T.; Zhu, Y.; Adzic, R. R. *Angew. Chem. Int. Ed. Engl.* **2012**, *51*, 6131–6135.

(27) McKone, J. R.; Sadtler, B. F.; Werlang, C. A.; Lewis, N. S.; Gray, H. B. *ACS Catal.* **2013**, *3*, 166–169.

(28) Sun, T.; Zhang, C.; Chen, J.; Yan, Y.; Zakhidov, A. A.; Baughman, R. H.; Xu, L. *J. Mater. Chem. A* **2015**, *3*, 11367–11375.

(29) Jiang, T.; Poyraz, A. S.; Iyer, A.; Zhang, Y.; Luo, Z.; Zhong, W.; Miao, R.; El-Sawy, A. M.; Guild, C. J.; Sun, Y.; Kriz, D. A.; Suib, S. L. *J. Phys. Chem. C* **2015**, *119*, 10454–10468.

(30) Kibsgaard, J.; Chen, Z.; Reinecke, B. N.; Jaramillo, T. F. *Nat. Mater.* **2012**, *11*, 963–969.

(31) Kim, O.-H.; Cho, Y.-H.; Kang, S. H.; Park, H.-Y.; Kim, M.; Lim, J. W.; Chung, D. Y.; Lee, M. J.; Choe, H.; Sung, Y.-E. *Nat. Commun.* **2013**, *4*, 2473.

(32) Ma, T. Y.; Dai, S.; Jaroniec, M.; Qiao, S. Z. *J. Am. Chem. Soc.* **2014**, *136*, 13925–13931.

(33) Xing, Z.; Liu, Q.; Asiri, A. M.; Sun, X. *Adv. Mater.* **2014**, *26*, 5702–5707.

(34) Xie, J.; Zhang, H.; Li, S.; Wang, R.; Sun, X.; Zhou, M.; Zhou, J.; Lou, X. W. D.; Xie, Y. *Adv. Mater.* **2013**, *25*, 5807–5813.

(35) Cheng, F.; Zhang, T.; Zhang, Y.; Du, J.; Han, X.; Chen, J. *Angew. Chem. Int. Ed. Engl.* **2013**, *52*, 2474–2477.

(36) Dieterle, M.; Weinberg, G.; Mestl, G. *Phys. Chem. Chem. Phys.* **2002**, *4*, 812–821.

(37) Skúlason, E.; Tripkovic, V.; Björketun, M. E.; Gudmundsdóttir, S.; Karlberg, G.; Rossmeisl, J.; Bligaard, T.; Jónsson, H.; Nørskov, J. K. *J. Phys. Chem. C* **2010**, *114*, 18182–18197.

(38) Conway, B. E.; Tilak, B. V. *Electrochim. Acta* **2002**, *47*, 3571–3594.

(39) Morales-Guio, C. G.; Stern, L.-A.; Hu, X. *Chem. Soc. Rev.* **2014**, *43*, 6555–6569.

(40) Bockris, J. O.; Potter, E. C. *J. Electrochem. Soc.* **1952**, *99*, 169–186.

(41) Lukowski, M. A.; Daniel, A. S.; Meng, F.; Forticaux, A.; Li, L.; Jin, S. *J. Am. Chem. Soc.* **2013**, *135*, 10274–10277.

(42) Lukowski, M. A.; Daniel, A. S.; English, C. R.; Meng, F.; Forticaux, A.; Hamers, R. J.; Jin, S. *Energy Environ. Sci.* **2014**, *7*, 2608–2613.

CHAPTER 4. STRUCTURE-PROPERTY RELATIONSHIP OF COPPER MODIFIED MESOPOROUS TiO_2 MATERIALS ON ALKYNE HOMOCOUPLING REACTION

4.1 Introduction

1,3-Diyne is a pharmaceutical and bioactive compound that occurs in numerous natural products. 1,3-Diyne compounds have been widely used in antibacterial, antifungal, anti-HIV, and pesticide applications.[1,2] Given the significance, synthesis of 1,3-Diyne has attracted quite a bit of attention. The most widely used procedure for preparing symmetrical diynes is the oxidative alkyne homocoupling reaction.[3] Generally, the metal catalyzed homocoupling of terminal alkynes is the most efficient route. Due to the efficiency and mildness, the combination of palladium (Pd) and copper salts is the most straightforward process for homocoupling reactions.[4,5,6] However, the high cost of Pd and the air-sensitive experimental conditions limit their wider applicability. Another concern is most of the reported systems are homogeneous and have shortcomings such as the difficulty of catalyst/product separation and the reusability.[7,8] Among the heterogeneous systems, copper based catalysts [CuI, CuCl, $Cu(OH)_2$, $Cu(OAc)_2$ *etc*.] with appropriate additives and oxygen as an oxidizing agent have been applied for homocoupling.[9,10,11,12] Although the copper catalyzed homocoupling system has been studied in decades, , the development of efficient heterogeneous systems for homocoupling reaction without any additives still poses a challenge from economic and environmental viewpoints.[13,14] Moreover, it is not

efficient to use copper materials without any supports based on previous studies.[15]

Herein, we prepared the copper modified TiO_2 materials via three different methods to achieve different Cu species. The mesoporous TiO_2 support was prepared by using previously developed UCT method.[16] The incorporation of copper mainly through three ways: doping, solvent free, and impregnation methods. In the doping method, a copper source [$Cu(NO_3)_2$] was added to the titanium source simultaneously in the beginning of the synthesis. As a result, copper appears as Cu^+ species in the TiO_2 lattice. For the solvent free and the impregnation methods, the copper source was incorporated with prepared TiO_2 powders with or without solvent (butanol), respectively. As a consequence, copper exists as CuO species on the TiO_2 surface. This study compared the different homocoupling catalytic activities of different copper species with the same mesoporous TiO_2 support. Special attention was paid to study the structure-property relationship on the catalytic activity. Our studies suggest that the highest homocoupling catalytic activity is attributed to the large surface area, appropriate pore size, and the existence of Cu (I) species.

4.2. Experimental Section

4.2.1. Catalyst preparation

The mesoporous TiO_2 material was prepared based on previously developed UCT inverse micelle templated sol-gel approach.[16] The copper source was incorporated into the mesoporous TiO_2 system by using three different methods: doping, solvent free, and impregnation methods.

In the doping method, X mol $Cu(NO_3)_2 \cdot 3H_2O$ (X = 0.0005, 0.001, 0.0015 mol) was added into titanium precursor solution [0.01 mol (2.84 g) of titanium isopropoxide was dissolved in a solution containing 0.094 mol (7 g) of 1-butanol, 0.016 mol (1 g) of HNO_3 and 1.72×10^{-4} mol of P123 surfactant in a 150 mL beaker at room temperature (RT)]. A clear bright blue gel was obtained after 30 min of magnetic stirring and was then placed in an oven at 120°C for 4 h. For all doped samples, the obtained dark green, transparent (rigid) films were calcined in a furnace under air at 450°C for 4 h. The doped samples were labeled as M%Cu-TiO_2-D, where M is the mol% of copper (M= 5, 10, 15%), D is the abbreviation of dope.

In the solvent free method, mesoporous TiO_2 was first prepared without incorporating any copper source. The achieved TiO_2 powder was mixed together with $Cu(NO_3)_2 \cdot 3H_2O$ in an agate mortar, with a different molar ratio (Cu/Ti = 5, 10, 15 mol%) for 30 min. The obtained mixture was then calcined in a furnace under air at 450°C for 4 h. The solvent free samples were labeled as M%Cu-TiO_2-SF, where M is the mol% of copper (M= 5, 10, 15%).

In the impregnation method, mesoporous TiO_2 was first prepared without incorporating any copper source. The achieved TiO_2 powder was introduced into a beaker containing 3 mL aqueous solution of $Cu(NO_3)_2 \cdot 3H_2O$, the Cu/Ti ratios were kept at 5, 10, and 15%. After stirring for 3 h, the mixture solution was dried overnight in an 80 °C oven. The obtained light blue powder was then calcined in a furnace under air at 450°C for 4 h. The impregnation samples were labeled as M%Cu-TiO_2-IMP, where M is the mol% of

copper (M= 5, 10, 15%).

4.2.2. Characterization

Powder X-ray diffraction (PXRD) analyses were performed on a Rigaku Ultima IV diffractometer (Cu Kα radiation, λ=1.5406 A) with an operating voltage of 40 kV and a current of 44 mA. Nitrogen (N_2) sorption experiments were conducted on a Quantachrome Autosorb-1-1C automated sorption system. The powders were degassed at 150°C for 3 h prior to the measurements. The surface areas were calculated by the Brunauer-Emmett-Teller (BET) method and the pore size distributions were calculated by the Barrett-Joyner-Halenda (BJH) method from the desorption isotherm. Morphological characterization was done using an FEI Nova NanoSEM 450 with an accelerating voltage of 2.0 kV. Energy dispersive X-ray spectroscopy (EDX) was performed on an Oxford Aztec Energy microanalysis system with an X-Max 80 silicon drift detector. X-ray photoelectron spectroscopy (XPS) measurements were performed in a PHI model 590 spectrometer with multiprobes (ΦPhysical Electronics Industries Inc.), using Al Kα radiation (λ=1486.6 eV) operated at 250 W. The shift of binding energy due to relative surface charging was corrected using the C 1s level at 284.6 eV as an internal standard.

4.2.3. Catalytic activity measurements

A typical procedure for alkyne homocoupling reaction is as follows: a mixture of phenylacetylene (0.5 mmol), M%Cu-TiO_2 catalysts (50 mg), and toluene (3 mL) was added in a 25 mL round-bottom flask equipped with a condenser. The reaction mixture was heated to reflux under vigorous stirring (600 rpm) for the required time (1-3 h). After reaction, the

catalyst was removed by filtration. The liquid product was collected and analyzed by GC/MS (gas chromatography/ mass spectrometry).

4.3. Results

4.3.1. Crystal Strcutures

To prepare copper based catalysts, previously reported UCT mesoporous TiO_2[16] was chosen as the support and copper nitrate [$Cu(NO_3)_2$] was used as copper precursor. The copper source was introduced into mesoporous TiO_2 systems via three different preparation methods (doping, solvent free, and impregnation). Different forms of copper (either present in the TiO_2 lattice, or as copper oxide on the TiO_2 surface) are expected. Besides the introduction methods of copper, all the other preparation processes are the same. Figure 4.1 shows the powder X-ray diffraction (PXRD) patterns of Cu-TiO_2 samples with different preparation methods: dope (Figure 4.1a), solvent free (Figure 4.1b), and impregnation (Figure 4.1c) methods. For each method, samples with different concentrations (5~15%) of copper were synthesized. As a comparison, the PXRD pattern of bare TiO_2 was plotted in each figure (Figure 4.1a-c). In Figure 4.1a, copper was introduced into TiO_2 structure as a dopant. With the increasing of copper content (0~15 %), the crystallinity of each sample did not significantly change. Compared to bare TiO_2 (black pattern), doped samples show no new diffraction lines that correspond to copper oxide species (CuO or Cu_2O), indicating the copper precursor (Cu^{2+}) was successfully doped into the TiO_2 lattice without change the bulk structure. However, by using the solvent free method (Figure 4.1b), the as-

synthesized Cu-TiO_2-SF samples possess different crystalline properties. In Figure 4.1b, new diffraction lines were observed in samples with higher copper concentration (10%Cu-TiO_2 SF, 15%Cu-TiO_2 SF), which can be indexed to (002) planes of CuO species.[17] With higher concentrations of copper, the (002) plane displays higher intensity, further manifesting the existence of CuO species. In Figure 4.1c, the Cu-TiO_2 samples prepared by impregnation methods exhibit similar crystalline properties with SF samples. Diffraction lines belonging to CuO species were observed. Moreover, the CuO species started to appear in the 5%Cu-TiO_2-IMP sample, due to the observation of a weak diffraction peak around 35.4° which are indexed to (002) planes of CuO.[18] In summary, by comparing these three types of Cu-TiO_2 samples, copper oxide (CuO) species can be most easily prepared via impregnation methods. No copper oxide can be observed in any of the doped samples.

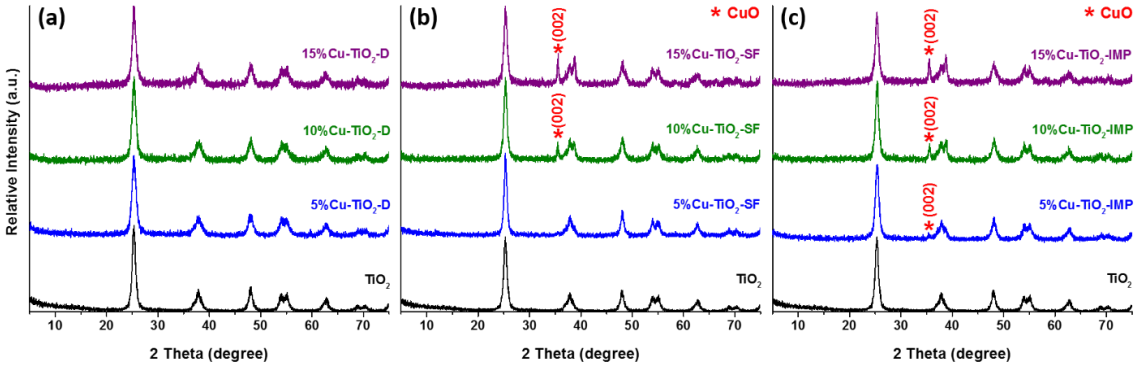

Figure 4. 1 Cu-TiO_2 samples with various copper loading amount (0~15 mol%, from bottom to top pattern) prepared by different methods: (a) doping method, (b) solvent free method, and (c) impregnation method.

4.3.2. Morphology and Surface Species Studies

Not only the crystal structures of Cu-TiO_2 samples are significantly different, but also the morphologies of each sample are distinct. According to the SEM image (Figure 4.2a), the 10%Cu-TiO_2-D sample displays a relatively smooth surface, without the deposition of copper oxide species (CuO, Cu_2O) on the surface. The copper source (Cu^{2+}) may be introduced into TiO_2 lattice as a dopant. However, both 10%Cu-TiO_2-SF (Figure 4.2b) and 10%Cu-TiO_2-IMP (Figure 4.2c) show rough surfaces, with clusters of particles deposited on the surface, which may refer to the coper oxide species. With higher magnification, a porous structure can be observed for the 10%Cu-TiO_2-D sample (Figure 4.2d). Pores with diameters around 100 nm are well dispersed on the surface of TiO_2. No pores could be detected with the same magnification of 10%Cu-TiO_2-SF (Figure 4.2e) or 10%Cu-TiO_2-IMP (Figure 4.2f) samples. The surfaces of these two samples were covered with copper oxide species. The SEM results are in agreement with the XRD results, no copper oxide species were detected for the 10%Cu-TiO_2-D sample. Copper oxide (CuO) only appears in the 10%Cu-TiO_2-SF and 10%Cu-TiO_2-IMP samples.

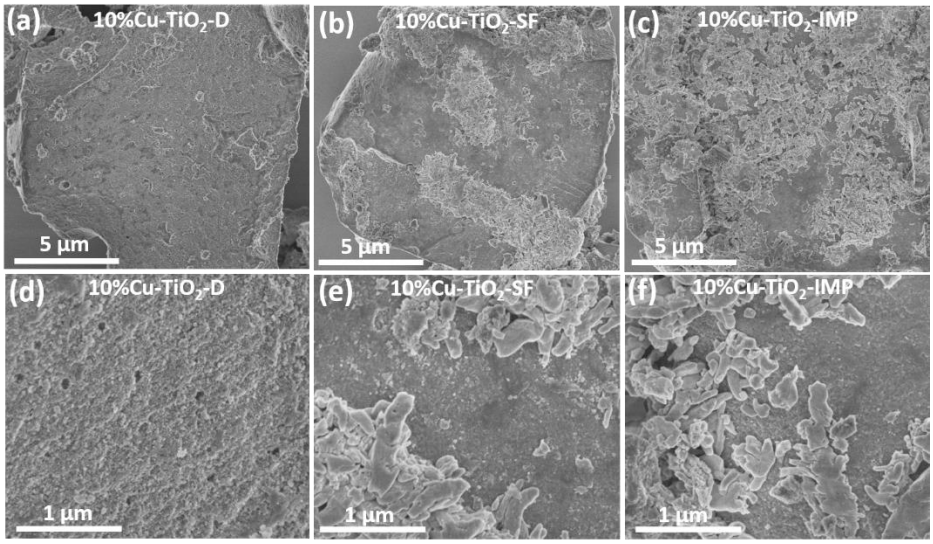

Figure 4. 2 Scanning electron microscopy (SEM) images of 10%Cu-TiO_2-D, 10%Cu-TiO_2-SF, and 10%Cu-TiO_2-IMP samples. Different scales of magnification were used: (a)-(c) 5 µm; (d)-(f) 1 µm.

The EDX element mapping technique was further applied to study the dispersion of copper. The element mapping of O, Ti, and Cu are shown in Figure 4.3. Figure 4.3a shows that all the elements are distributed uniformly in the whole test area, indicating that Cu existed in an orderly way and uniformly throughout the TiO_2 lattice of the 10%Cu-TiO_2-D sample. The map of O, Ti, and Cu elements fits the sample morphology, in accordance with XRD (Figure 4.1a) and SEM results (Figure 4.2). No separate CuO species appear on the surface of TiO_2. In 10%Cu-TiO_2-SF (Figure 4.3b) and 10%Cu-TiO_2-IMP (Figure 4.3c) samples, copper is present in the area where there is less titanium. A phenomenon of mutual exclusion was observed between TiO_2 and CuO species. In the element mapping of 10%Cu-TiO_2-IMP, especially in the area of CuO gathered, only a very weak Ti signal was detected. Thus, the clusters that deposited on the surface (Figure 4.2e, f) of 10%Cu-TiO_2-SF and 10%Cu-TiO_2-IMP samples can be determined as CuO species that are present separately from the TiO_2 lattice.

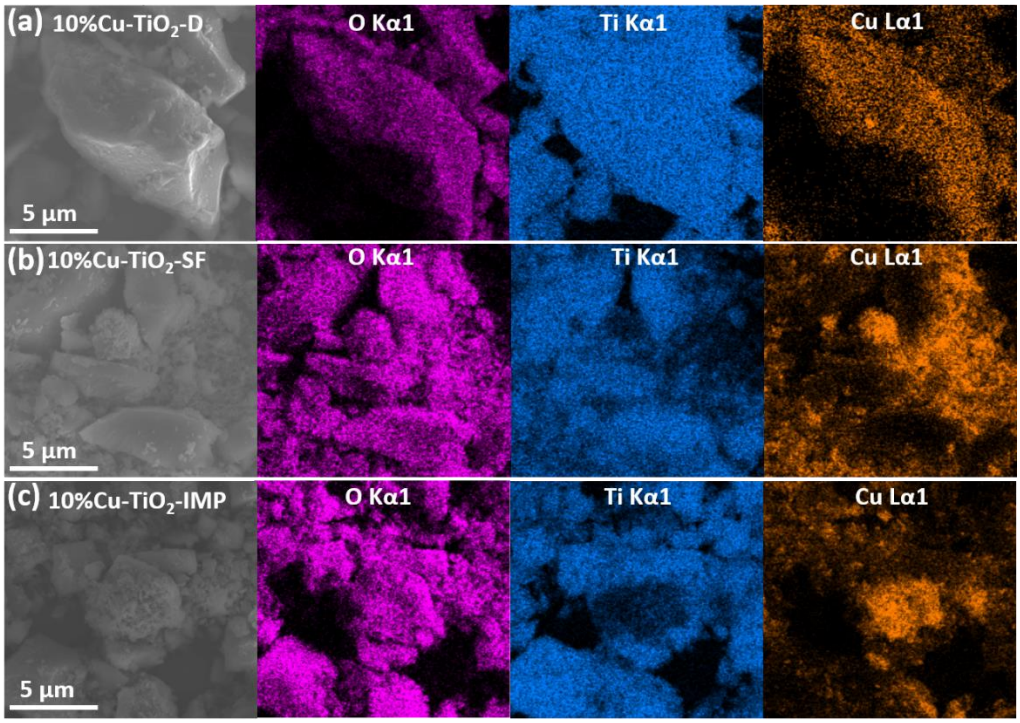

Figure 4. 3 SEM images with EDX element mapping results of as-prepared (a) 10%Cu-TiO_2-D, (b) 10%Cu-TiO_2-SF, and (c) 10%Cu-TiO_2-IMP samples. Oxygen, titanium, and copper elements were mapped. Scale bars of all images are 5µm.

4.3.3. Porosity and Pore Size Distribution

The N_2 adsorption-desorption isotherms and the BJH pore size distribution plots of prepared mesoporous TiO_2 and all Cu-TiO_2 samples are displayed in Figure 4.4. All the isotherms show the typical Type IV isotherm, which is a characteristic type of mesoporous material. The bare mesoporous TiO_2 (Figure 4.4a) has a hysteresis loop close to Type H2, which usually refers to an ink-bottle pore with a pore connecting to a smaller pore.[19] With the introduction of Cu into TiO_2 system, the hysteresis loops of all Cu-TiO_2 samples are different, suggesting the different pore shape, network, and distribution status. The 10%Cu-TiO_2-D sample (Figure 4.4b) has two hysteresis loops, indicating a bimodal pore size distribution in the mesoporous (2-50 nm) and macroporous (> 50 nm) regions. The inset image of Figure 4.4b shows that the BJH pore size distribution in the mesoporous region of 10%Cu-TiO_2-D (4.9 nm) is bigger than bare TiO_2 (3.4 nm), implying the impact of Cu on the TiO_2 structure. The hysteresis loop of 10%Cu-TiO_2-D in the 0.7-0.9 p/p_0 range suggests another pore size distribution in the macroporous region, which is in accordance with SEM results. The macropore sizes of 10%Cu-TiO_2-D that were measured from SEM image (Figure 4.2d) are around 80 nm. In contrast, the isotherms and the hysteresis loops of 10%Cu-TiO_2-SF and 10%Cu-TiO_2-IMP samples (Figure 4.4c, d) are not too different as compared to bare TiO_2. The BJH pore size distributions were preserved (3.4 nm) after Cu incorporation. Above all, among all the Cu-TiO_2 samples, the doped Cu system possesses the biggest structural change compared to bare TiO_2.

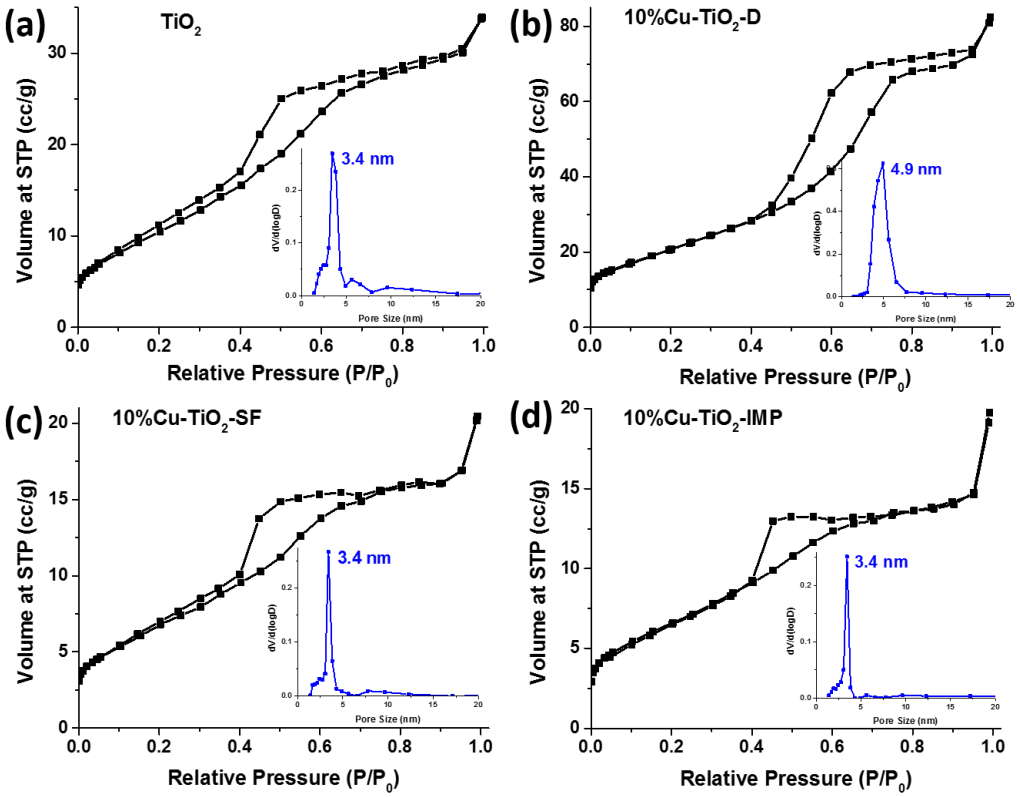

Figure 4. 4 N_2 sorption isotherms for (a) bare TiO_2, (b) 10%Cu-TiO_2-D, (c) 10%Cu-TiO_2-SF, and (d) 10%Cu-TiO_2-IMP. The inset figures are the BJH desorption pore-size distribution for each sample (a) 3.4 nm, (b) 4.9 nm, (c) 3.4 nm, and (d) 3.4 nm.

4.3.4. Surface Compositions and Oxidation States

The surface compositions and oxidation states of all Cu-TiO_2 samples were studied by X-ray photoelectron spectroscopy (XPS) analysis. The corresponding experimental results are displayed in Figure 4.5. As shown in Figure 4.5a, the peaks with the highest intensity can be assigned to Cu $2p_{3/2}$ and the peaks in the region of 952-954 eV are attributed to Cu $2p_{1/2}$.[20] The 10%Cu-TiO_2-D sample exhibits two main peaks at 931.2 and 951.2 eV corresponding to the Cu $2p_{3/2}$ and Cu $2p_{1/2}$ levels of Cu^+ state, respectively.[21] Compared to 10%Cu-TiO_2-D sample, clear shifts toward higher binding energy level were achieved from 10%Cu-TiO_2-SF and 10%Cu-TiO_2-IMP samples. The Cu $2p_{3/2}$ and Cu $2p_{1/2}$ levels of both samples are attributed to the Cu^{2+} state (CuO). Moreover, broad satellite peaks at 943-945 eV can be observed in 10%Cu-TiO_2-SF and 10%Cu-TiO_2-IMP samples, both of which can be indexed to the presence of the Cu^{2+} state (CuO) on the surface.[22] The binding energies of O 1s results (Figure 4.5b) were analyzed to further study the chemical compositions. With the binding energy of 530.4 eV, the O 1s peak of 10%Cu-TiO_2-D sample was attributed to Cu_2O lattice oxygen.[23] The O 1s binding energy levels of 10%Cu-TiO_2-SF and 10%Cu-TiO_2-IMP samples are slightly lower than 10%Cu-TiO_2-D, a clear shift towards lower energy level can be observed in Figure 4.5b. As shown in the literature, the O 1s energy level of 529.2-529.9 eV can be assigned to CuO lattice oxygen.[24] The study of O 1s spectra further manifests that Cu^+ only exists in 10%Cu-TiO_2-D sample.

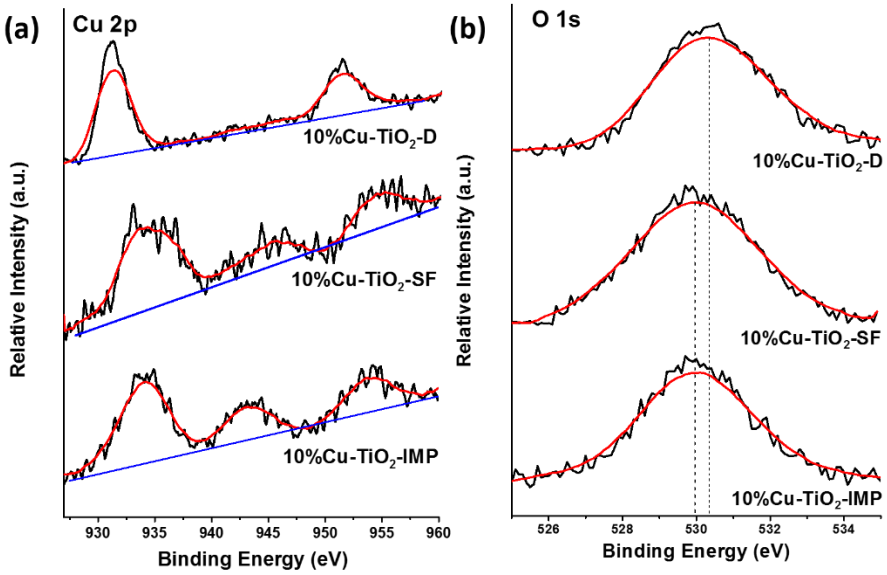

Figure 4. 5 XPS spectra details for (a) Cu 2p binding energy regions, (b) O 1s level for 10%Cu-TiO_2-D, 10%Cu-TiO_2-SF, and 10%Cu-TiO_2-IMP samples (from top to bottom).

4.3.5. Catalytic Studies

The catalytic activities of all prepared catalysts were tested by the homocoupling reaction of phenylacetylene (**1a**) to 1,4-diphenyl-1,3-butadiyne (**1b**). All catalysts were compared in toluene under ambient atmosphere at 110 °C (Table 4.1). The focus of this study was to study how the copper concentration and the chemical status of copper affect the catalytic activity. Thus, catalysts with different concentration of copper and with various preparation methods were tested. First, a control experiment without any catalysts was conducted. No significant amount of **1b** product can be obtained (under GC detection, Table 4.1, entry 1). No reaction proceeded in the presence of bare mesoporous TiO_2, suggesting that TiO_2 does not have any active sites for alkyne homocoupling (Table 4.1, entry 2). However, after the introduction of copper into the TiO_2 system, the yields were significantly improved. In order to determine whether the homocoupling reaction is a time-dependent reaction, different reaction times were used (1-3 h). In Figure 4.6a, the **1b** product yield is linearly increasing with time. The effects of copper concentration were then investigated. As shown in Figure 4.6b, with higher concentration of copper, the Cu-TiO_2-D catalysts show better catalytic activity. In contrast, for Cu-TiO_2-SF catalysts, higher copper concentration brings lower yields (Figure 4.6c). Moreover, the copper concentration is not a key factor for the Cu-TiO_2-IMP sample (Figure 4.6d). With higher amounts of copper, no obvious increase or decrease in catalytic activity can be observed. Above all, copper is a critical factor for the homocoupling reaction, but the increasing concentration of copper does not consequently bring higher yield.

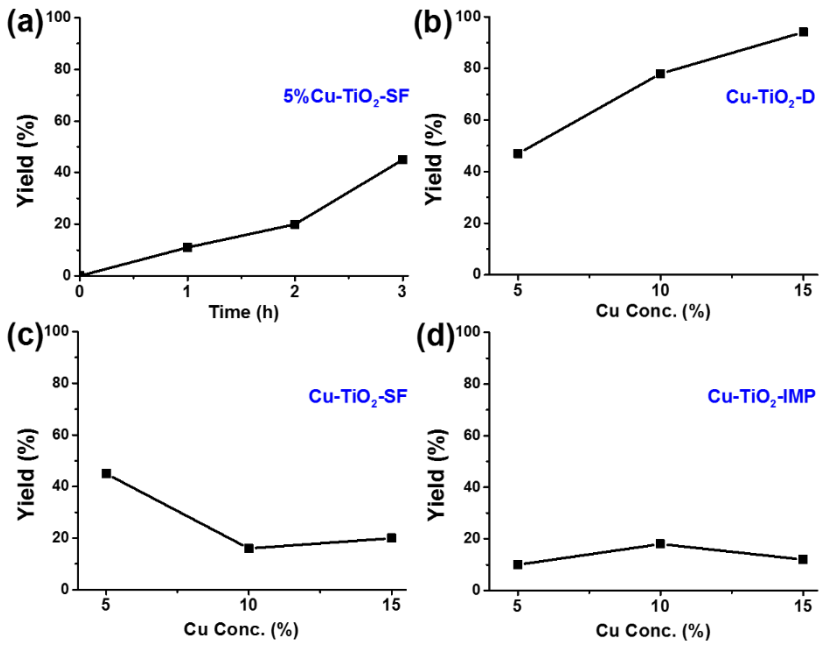

Figure 4. 6 (a) Results of yield as a function of reaction time (0-3 h) by using solvent free method prepared catalyst (10%Cu-TiO_2-SF). Results of yield as a function of copper loading amounts (0-15 mol%) of samples prepared by different methods: (b) doping, (c) solvent free, and (d) impregnation methods.

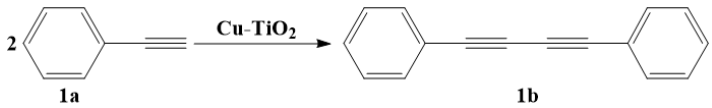

Table 4. 1 Homocoupling of phenylacetylene (1a) by various catalysts.[a]

Entry	Catalyst	Time	Yield **2a**
1	None	3	nd
2	TiO_2	3	nd
3	5%Cu-TiO_2-SF	1	11
4	5%Cu-TiO_2-SF	2	20
5	5%Cu-TiO_2-SF	3	45
6	10%Cu-TiO_2-SF	3	16
7	15%Cu-TiO_2-SF	3	20
8	5%Cu-TiO_2-D	3	47
9	10%Cu-TiO_2-D	3	78
10	15%Cu-TiO_2-D	3	94
11	5%Cu-TiO_2-IMP	3	10
12	10%Cu-TiO_2-IMP	3	18
13	15%Cu-TiO_2-IMP	3	12
14	10%Cu-TiO_2-D 350	3	>99

[a] Reaction conditions: **1a** (0.5 mmol), catalyst (50 mg), toluene (3 mL), 110 °C, under ambient atmosphere. Yields were determined by GC. nd = not detected (below 1 % yield).

4.4. Discussion

4.4.1. Cu (I) and Cu (II) active sites

Copper is regarded as the active site since bare TiO_2 shows no catalytic activity during alkyne homocoupling process. Both Cu (I) and Cu (II) species have been reported as active sites for alkyne homocoupling reaction. Supported Cu (II) salts such as $Cu(OH)_2$, $Cu(OAc)_2$ H_2O, and $CuCl_2$ serve as homocoupling catalysts that have been reported previously.[25, 26] Oishi et al. proposed a rapid electron-transfer path that use MnO_2 supported Cu (II) species as the homocoupling catalyst.[27] Cu (II) will be reduced to Cu (I) during coupling process. The support (MnO_2) would not only act as a support but also an electron acceptor that oxidizes Cu (I) back to Cu (II). Subsequently the reduced Mn_2O_3 species are further oxidized to MnO_2 by O_2. In this study, in terms of XPS results (Figure 4.5a), Cu (II) exists in 10%Cu-TiO_2-SF and 10%Cu-TiO_2-IMP samples. The electron-transfer path should also occur in these two samples. However, the reaction rate of these two samples are much slower than the reported Cu (II)/MnO_2 sample. Despite the different experimental conditions, the main difference is the support. Compared to manganese, titanium has lower electronegativity, which means Ti^{4+} is more difficult to attract an electron to form Ti^{3+}. During the homocoupling reaction, Cu (II) was reduced to Cu (I), forming a free electron. If the free electron cannot be rapidly accepted by Ti^{4+} to form Ti^{3+}, the entire reaction rate will be significantly decreased. This is the reason why 10%Cu-TiO_2-SF (yield = 16%) and 10%Cu-TiO_2-IMP (yield = 18%) show very low yield in coupling reactions.

Supported Cu (I) salts were also reported as efficient catalysts for coupling reactions.

For example, copper (I)-modified zeolites were reported as efficient catalysts for the coupling reactions by behaving as an acidic Glaser-type catalyst.[28] In this pathway, the terminal alkyne will be dehydrogenated by a Cu ion and forming Cu (I) phenylacetylide intermediate.[1,29] By further exposing to oxygen, oxidative dimerization to diphenyldiacetylene can be obtained. In this study, based on XPS results (Figure 4.5a), Cu (I) exists in 10%Cu-TiO_2-D sample and catalyzes coupling reaction by following the Glaser mechanism. The proposed mechanism in 10%Cu-TiO_2-D system will be as follows. First the phenylacetylene particle dehydrogenates on the surface of the catalyst and binds with Cu (I) site. With further exposure to air, two adjacent Cu (I) phenylacetylide intermediates dimerize with each other and leave the surface of the catalyst. Without the redox reactions between Cu species (Cu^+/Cu^{2+}) and Ti species (Ti^{4+}/Ti^{3+}), the reaction rate in 10%Cu-TiO_2-D system is much higher than 10%Cu-TiO_2-SF or 10%Cu-TiO_2-IMP systems, which result in much higher yield (94 %). Above all, in terms of different forms of copper species, different homocoupling mechanisms were followed.

4.4.2. Materials properties, the decisive role of structure

Material (catalysts) properties, such as surface area, pore structure and morphologies significantly influence the catalytic activity in heterogeneous catalytic system. Generally, higher surface area brings more active sites, leading to higher catalytic activity. The surface areas of all samples have been determined by the Brunauer–Emmett–Teller (BET) theory. Compared to other samples, the 10%Cu-TiO_2-D has the largest surface area (60 m^2/g). In other words, with the same amount of catalysts in the homocoupling reactions, there will

be more active sites on the surface of 10%Cu-TiO_2-D than on the surface of 10%Cu-TiO_2-SF or 10%Cu-TiO_2-IMP samples. Therefore, 10%Cu-TiO_2-D exhibits higher catalytic activity.

Another key element is the porous structure of all samples. In the study of zeolite supported Cu materials, the larger the pore size, the higher the yield. This occurs because the pores are able to accommodate rod-shaped diynes.[30] In this study, all the prepared materials possess mesoporous structure, with different pore size distributions summarized in Table 4.1. Both the 10%Cu-TiO_2-SF and 10%Cu-TiO_2-IMP samples have a pore size distribution at 3.4 nm. This is relatively small compared to 10%Cu-TiO_2-D sample (4.9 nm). Mesopores are able to facilitate mass transport, the rod-shaped diynes can not only bind with the surface active sites, but also can be transported into the porous structure and can further interact with more active sites without blocking the pores. More importantly, according to SEM images (Figure 4.2a), 10%Cu-TiO_2-D also has macropores with a pore size around 80 nm. With the combination of mesopores and macropores, the reagent molecules can diffuse and be transported to larger surface of the catalysts. The catalytic activity was therefore improved.

Moreover, the effect of morphology of the material is also a critical factor for catalytic performance. The differences of morphologies of all the prepared catalysts can be clearly seen from the SEM images (Figure 4.2). These differences are attributed to the different preparation methods and the differently formed copper species. The sample prepared via a doping method (10%Cu-TiO_2-D) has a relatively smooth surface, copper

exsits as Cu^{+} species in the TiO_2 lattice. In contrast, samples prepared via solvent free (10%Cu-TiO_2-SF) and impregnation (10%Cu-TiO_2-IMP) methods have large CuO clusters on the surface. The large size (3 – 10 μm) of these agglomerated CuO clusters impede the close contact between the active sites and TiO_2 support, which further depresses the catalytic activity. Especially for samples prepared via solvent free methods (Cu-TiO_2-SF), as shown in Figure 6c, with higher loading of copper, the catalytic activity is lower since high metal loadings favor particle agglomeration.[31] The surface agglomeration of CuO species gives rise to a series of negative consequences, such as reduced surface area, blocked pores and undesired phase transformation, which cause a significant decrease in catalytic performance.[32]

To further prove that the above-discussed factors are critical for the homocoupling reaction, a sample with higher surface area, appropriate pore size and smooth surface morphology was prepared and tested in homocoupling reactions. Based on the above catalytic results (Table 4.1), we chose the doping method as the preparation procedure, due to its highest catalytic activity. A lower calcination temperature (350 °C) was used to achieve enhanced properties. As shown in Figure 7a, 10%Cu-TiO_2-D/350 sample exhibits the Type IV isotherm and the pore size distribution is in the mesopores range (2-50 nm), but with much higher surface area (128 m^2/g) than all other samples. The morphological properties (Figure 4.7a) are similar to 10%Cu-TiO_2-D sample, relatively smooth surface and well dispersed macropores. Most importantly, copper is well dispersed in the TiO_2 lattice in terms of EDX elemental mapping results (Figure 4.7c). The catalytic activity of

10%Cu-TiO_2-D/350 sample was tested under identical conditions with all other samples and the result shows the highest activity (> 99% yield, Table 1, entry 14). All the properties of 10%Cu-TiO_2-D/350 sample were in accordance with the above discussed prerequisites for a high catalytic activity, further suggesting the decisive role of the material structure during the catalytic reaction.

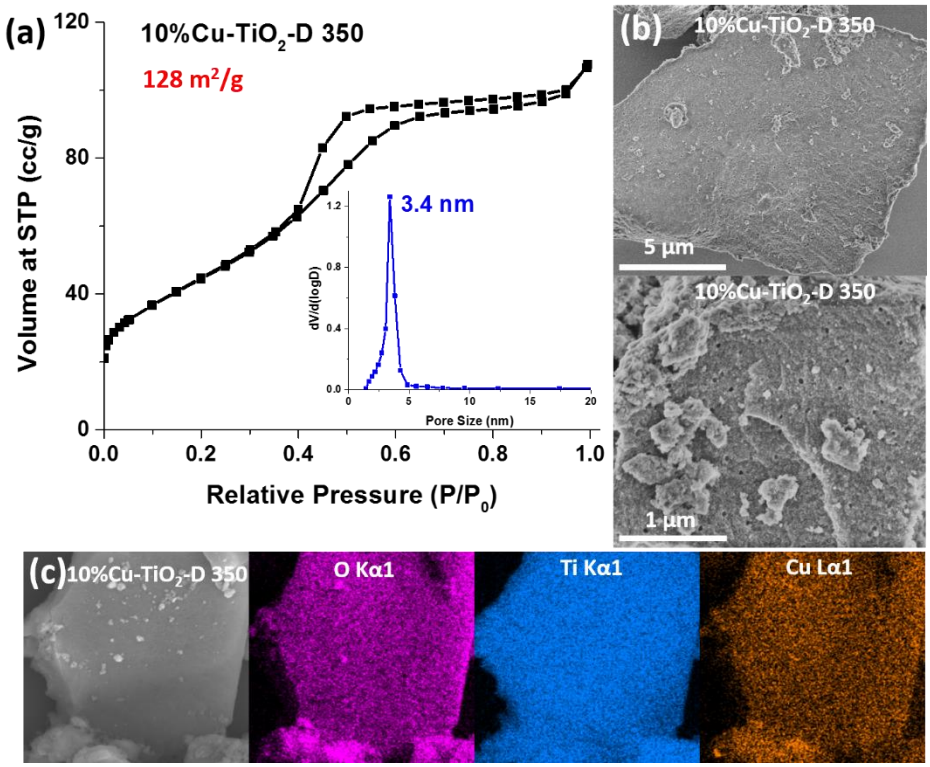

Figure 4. 7 Characterization of 10%Cu-TiO_2-D/350 sample by using (a) N_2 sorption (onset image: BJH pore size distribution at 3.4 nm); (b) SEM images with different scale bars (1, 5 µm); (c) EDX element mapping of oxygen, titanium, and copper elements.

4.4.3. The stability and recyclability

Stability is one of the most important evaluations for the catalyst. Thus, after beting tested by the homocoupling reaction, all the catalysts were collected, dried, and characterized by PXRD and EDX element mapping. All the PXRD patterns are shown in **Figure 4.8a**. Compared to XRD patterns of as-synthesized samples (**Figure 4.1**), no new or missing diffraction lines can be observed, indicating all the samples preserved their crystallinity and crystal structure. The diffraction lines of CuO species in 10%Cu-TiO_2-SF and 10%Cu-TiO_2-IMP samples were also preserved after the homocoupling reaction, manifesting the stability of CuO species during the catalytic reaction. The high dispersion of copper was preserved in all samples after reaction in comparison to as-prepared samples (**Figure 4.3**) and no obvious agglomeration occurred. The recyclability tests were carried out by reusing the recycled catalyst from a previous run. The 10%Cu-TiO_2-D/350 sample was retrieved by filtration and dried in ambient air with no washing or reactivation processes (**Figure 4.8b**). After the three cycles of the reaction, most of the catalytic activity was preserved (yield = 74%). The small loss of catalytic activity may be due to the loss of copper active sites.

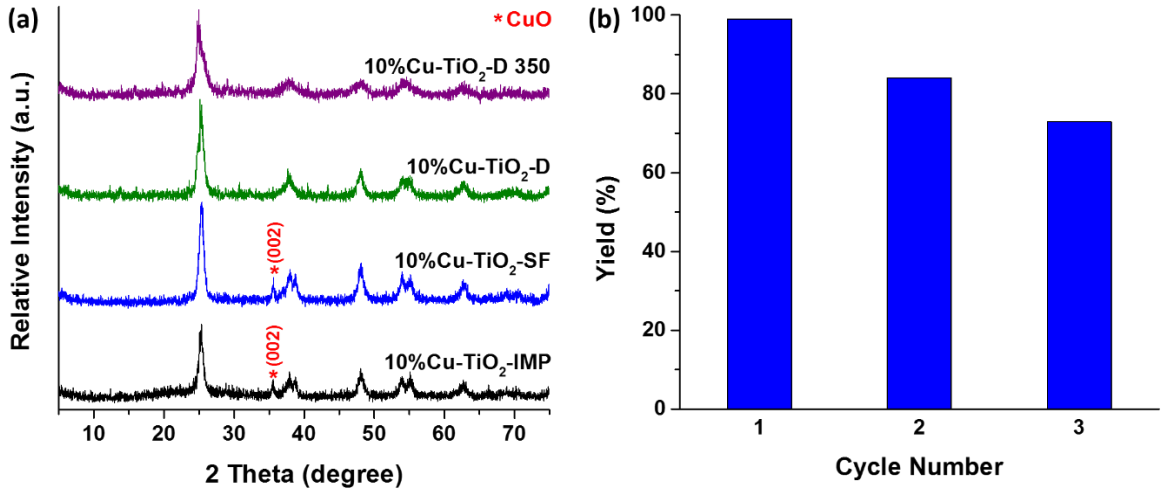

Figure 4. 8 (a) PXRD patterns of all samples collected after homocouling reaction. (b) The recyclability tests of 10%Cu-TiO_2-D/350 material (reaction temperature: 110 °C, reaction time: 3 h, 50 mg of catalyst).

4.5. Conclusions

In this study, a series of copper modified TiO_2 materials were prepared via three methods: doping (Cu-TiO_2-D), solvent free (Cu-TiO_2-SF), and impregnation (Cu-TiO_2-IMP) methods. Copper appears as Cu^+ species in the TiO_2 lattice of Cu-TiO_2-D samples. While copper is presents as CuO species on the TiO_2 surface in Cu-TiO_2-SF and Cu-TiO_2-IMP samples. Through the catalytic tests on the homocoupling of terminal alkynes reactions, copper doped TiO_2 sample (Cu-TiO_2-D) shows much higher activity (yield= 94%) than the other samples (Cu-TiO_2-SF or Cu-TiO_2-IMP). The 1,4-diphenyl-1,3-butadiyne yield increases with higher loading amount (0-15%) of copper only in the doped samples. Based on all the experimental results and discussion, large surface area, combination of mesopores (≈ 4 nm) and macropores (≈ 80 nm), and Cu (I) species as active sites are the key factors for high catalytic activity. The 10%Cu-TiO_2-D/350 sample, which has the highest surface area (128 m^2/g) and two pore size distributions shows the highest yield (> 99%) compared to all other samples with identical reaction conditions. The majority of the high yield (74%) was preserved even after three cycles.

4.6. References

(1) Glaser, C. *Berichte der Dtsch. Chem. Gesellschaft* **1869**, *2*, 422–424.

(2) Kamata, K.; Yamaguchi, S.; Kotani, M.; Yamaguchi, K.; Mizuno, N. *Angew. Chem. Int. Ed. Engl.* **2008**, *47*, 2407–2410.

(3) Wang, D.; Li, J.; Li, N.; Gao, T.; Hou, S.; Chen, B. *Green Chem.* **2010**, *12*, 45–48.

(4) Lei, A.; Srivastava, M.; Zhang, X. *J. Org. Chem.* **2002**, *67*, 1969–1971.

(5) Fairlamb, I. J. S.; Bäuerlein, P. S.; Marrison, L. R.; Dickinson, J. M. *Chem. Commun.* **2003**, 632–633.

(6) Batsanov, A. S.; Collings, J. C.; Fairlamb, I. J. S.; Holland, J. P.; Howard, J. A. K.; Lin, Z.; Marder, T. B.; Parsons, A. C.; Ward, R. M.; Zhu, J. *J. Org. Chem.* **2005**, *70*, 703–706.

(7) Herrmann, W. A.; Böhm, V. P. .; Gstöttmayr, C. W. .; Grosche, M.; Reisinger, C.-P.; Weskamp, T. *J. Organomet. Chem.* **2001**, *617-618*, 616–628.

(8) Auer, S. M.; Schneider, M.; Baiker, A. *J. Chem. Soc. Chem. Commun.* **1995**, 2057–2058.

(9) Siemsen, P.; Livingston, R.; Diederich, F. *Angew. Chem. Int. Ed. Engl.* **2000**, *39*, 2632–2657.

(10) Allen, S. E.; Walvoord, R. R.; Padilla-Salinas, R.; Kozlowski, M. C. *Chem. Rev.* **2013**, *113*, 6234–6458.

(11) Wendlandt, A. E.; Suess, A. M.; Stahl, S. S. *Angew. Chem. Int. Ed. Engl.* **2011**, *50*, 11062–11087.

(12) Liu, C.; Zhang, H.; Shi, W.; Lei, A. *Chem. Rev.* **2011**, *111*, 1780–1824.

(13) Gonzalez-Arellano, C.; Balu, A. M.; Luque, R.; Macquarrie, D. J. *Green Chem.* **2010**, *12*, 1995–2002.

(14) Alonso, F.; Melkonian, T.; Moglie, Y.; Yus, M. *European J. Org. Chem.* **2011**, *2011*, 2524–2530.

(15) Yamaguchi, K.; Wang, Y.; Oishi, T.; Kuroda, Y.; Mizuno, N. *Angew. Chem. Int. Ed. Engl.* **2013**, *52*, 5627–5630.

(16) Luo, Z.; Poyraz, A. S.; Kuo, C.-H.; Miao, R.; Meng, Y.; Chen, S.-Y.; Jiang, T.; Wenos, C.; Suib, S. L. *Chem. Mater.* **2015**, *27*, 6–17.

(17) Francisco, M. S. P.; Mastelaro, V. R. *Chem. Mater.* **2002**, *14*, 2514–2518.

(18) Wang, W.; Zhan, Y.; Wang, G. *Chem. Commun.* **2001**, 727–728.

(19) Chen, Z.; Cummins, D.; Reinecke, B. N.; Clark, E.; Sunkara, M. K.; Jaramillo, T. F. *Nano Lett.* **2011**, *11*, 4168–4175.

(20) Wang, Z.; Liu, Y.; Martin, D. J.; Wang, W.; Tang, J.; Huang, W. *Phys. Chem. Chem. Phys.* **2013**, *15*, 14956–14960.

(21) Ghijsen, J.; Tjeng, L. H.; van Elp, J.; Eskes, H.; Westerink, J.; Sawatzky, G. A.; Czyzyk, M. T. *Phys. Rev. B* **1988**, *38*, 11322–11330.

(22) Lee, Y. S.; Chua, D.; Brandt, R. E.; Siah, S. C.; Li, J. V; Mailoa, J. P.; Lee, S. W.; Gordon, R. G.; Buonassisi, T. *Adv. Mater.* **2014**, *26*, 4704–4710.

(23) Laibinis, P. E.; Whitesides, G. M. *J. Am. Chem. Soc.* **1992**, *114*, 9022–9028.

(24) Amri, A.; Duan, X.; Yin, C.-Y.; Jiang, Z.-T.; Rahman, M. M.; Pryor, T. *Appl. Surf. Sci.* **2013**, *275*, 127–135.

(25) Alonso, F.; Yus, M. *ACS Catal.* **2012**, *2*, 1441–1451.

(26) Jia, X.; Yin, K.; Li, C.; Li, J.; Bian, H. *Green Chem.* **2011**, *13*, 2175.

(27) Oishi, T.; Yamaguchi, K.; Mizuno, N. *ACS Catal.* **2011**, *1*, 1351–1354.

(28) Kuhn, P.; Alix, A.; Kumarraja, M.; Louis, B.; Pale, P.; Sommer, J. *European J. Org. Chem.* **2009**, *2009*, 423–429.

(29) Björk, J.; Zhang, Y.-Q.; Klappenberger, F.; Barth, J. V.; Stafström, S. *J. Phys. Chem. C* **2014**, *118*, 3181–3187.

(30) Kuhn, P.; Pale, P.; Sommer, J.; Louis, B. *J. Phys. Chem. C* **2009**, *113*, 2903–2910.

(31) Maillard, F.; Schreier, S.; Hanzlik, M.; Savinova, E. R.; Weinkauf, S.; Stimming, U. *Phys. Chem. Chem. Phys.* **2005**, *7*, 385–393.

(32) Tian, G.; Fu, H.; Jing, L.; Xin, B.; Pan, K. *J. Phys. Chem. C* **2008**, *112*, 3083–3089.

FUTURE WORK

In this work, several transition metal oxide materials have been prepared, characterized, and applied to various applications. The synthesis methods are able to create mesoporous, crystalline structure and with different crystal phases. The methods should not be limited to prepare the materials reported in this thesis. More oxides, such as Cr, V, Fe, Co, and Cu should be able to be synthesized. They have abundant inorganic sources and their metal ions are able to form metal-surfactant complexes in aqueous solution to prepare mesoporous materials. Their catalytic activities such as CO oxidation, selective oxidation hydrocarbon, and elimination of volatile organic compounds are worthy of study.

In the mesoporous mixed phase TiO_2 study, different metal dopants (Al, Cd, Co, Sn, and Cr) should be used. These metals have been reported as anatase-rutile phase transformation promoters. With the introduction of dopants, the TiO_2 based materials are expected to have visible light activity and can be further used in photocatalytic water splitting and photocatalytic CO_2 reduction systems.

In the hydrogen evolution study, the MoO_3 material can be prepared with different phases. The different phases (monoclinic, orthorhombic, or mixed phase) of the MoO_3 material should be fully characterized and the catalytic activity on hydrogen evolution reaction should be investigated.

In the copper catalyzed alkyne-alkyne homocoupling study, different mesoporous supports are worth trying. Mesoporous ZnO and ZrO_2 are appropriate candidates, due to their chemical stability as supports. Other homocoupling reactions that are based on copper

materials, such as the Ullmann reaction and the Gomberg-Bachmann reaction can be tested.

Appendix

List of Publications, Book Chapters, Patent Applications, Presentations, and Posters.

1. Journal Articles:

Zhu Luo, Altug S. Poyraz, Chung-Hao Kuo, Ran Miao, Yongtao Meng, Sheng-Yu Chen, Ting Jiang, Chelsea Wenos, Steven L. Suib; "Crystalline Mixed Phase (Anatase/Rutile) Mesoporous Titanium Dioxides for Visible Light Photocatalytic Activity" Chem. Mater. **2015**, *27,* 6–17.

Ben Liu, **Zhu Luo**, Anthony Federico, Wenqiao Song, Steven L. Suib, and Jie He; "Colloidal Amphiphile-Templated Growth of Highly Crystalline Mesoporous Nonsiliceous Oxides" Chem. Mater. **2015**, *27,* 6173-6176.

Ben Liu, Chung-Hao Kuo, Jiejie Chen, **Zhu Luo**, Srinivas Thanneeru, Weikun Li, Wenqiao Song, Sourav Biswas, Steven L. Suib, and Jie He; "Ligand-Assisted Co-Assembly Approach toward Mesoporous Hybrid Catalysts of Transition-Metal Oxides and Noble Metals: Photochemical Water Splitting" Angew. Chem. Int. Ed. **2015**, 54, 1-6.

Chung-Hao Kuo, Islam Mosa, Altug S. Poyraz, Sourav Biswas, Abdelhamid El-Sawy, Wenqiao Song, **Zhu Luo**, Sheng-Yu Chen, James F. Rusling, Jie He, Steven L. Suib; "Robust Mesoporous Manganese Oxide Catalysts for Water Oxidation" ACS Catalysis, **2015**, *5*, 1693-1699.

Yashan Zhang, Lei Jin, Kevin Sterling, **Zhu Luo**, Ting Jiang, Ran Miao, Curtis Guild, and Steven L. Suib; "Potassium Modiefied Layered $Ln_2O_2CO_3$ (Ln: La, Nd, Sm, Eu) Materials: Efficient and Stable Heterogeneous Catalysts for Biofuel Production" Green Chemistry,

2015, 17, 3600-3608.

Ting Jiang, Shoucheng Du, Tahereh Jafari, Wei Zhong, Yu Sun, Wenqiao Song, **Zhu Luo**, William A. Hines, Steven L. Suib; "Synthesis of Mesoporous γ-Fe2O3 Supported Palladium Nanoparticles and Investigation of Their Roles as Magnetically Recyclable Catalysts for Nitrobenzene Hydrogenation" Appl. Catal. A Gen., **2015**, 502, 105-113.

Ting Jiang, Altug S. Poyraz, Aparna Iyer, Yashan Zhang, **Zhu Luo**, Wei Zhong, Ran Miao, Abdelhamid El-Sawy, Curtis Guild, Yu Sun, David Kirz and Steven Suib; "Synthesis of Mesoporous Iron Oxide by an Inverse Micelle Method and Their Application in the Degradation of Orange II under Visible Light at Neutral pH" J. Phys. Chem. C, **2015**, 119, 10454-10468.

Chung-Hao Kuo, Weikun Li, Wenqiao Song, **Zhu Luo**, Altug S Poyraz, Yang Guo, Anson W K Ma, Steven L Suib, Jie He; "Facile synthesis of Co_3O_4@CNT with high catalytic activity for CO oxidation" ACS Appl. Mater. Interfaces. **2014**, *6*, 11311-11317.

Zhu Luo, Shaylin A. Cetegen, Ran Miao, Ting Jiang, Sheng-Yu Chen, Tahereh Jafari, Yashan Zhang, and Steven L. Suib; "Structure-Property Relationship of Copper Modified Mesoporous TiO_2 Materials on Alkyne Homocoupling Reaction" *Submitted*.

Zhu Luo, Tran Doan Huan, Islam M. Mosa, Altug S. Poyraz, Ran Miao, Wei Zhong, Jacqueline Cloud, David Kriz, Srinivas Thanneeru, Rampi Ramprasad and Steven L. Suib; " Mesoporous, Blue MoO_{3-x} Materials as Efficient Electrocatalyst for Hydrogen Evolution Reaction" *In preparation*.

2. Review

Stephen O. Hay, Timothy Obee, **Zhu Luo**, Ting Jiang, Yongtao Meng, Junkai He, Steven C. Murphy, and Steven Suib; "The viability of photocatalysis for air purification" Molecules, **2015**, *20*, 1319-1356.

3. Book Chapters

Homer C. Genuino, Nashaat Mazrui, Mohammad S. Seraji, **Zhu Luo**, George E. Hoag; New and Future Developments in Catalysis, "Green synthesized nano-scale iron for oxidative catalysis of organic environmental pollutants" **2013**, pp 41-61.

4. Patent

Zhu Luo, Steven L. Suib. Invention disclosur entitled "Preparation of Crystalline, Mesoporous Molybdenum Oxide and Its Application for Hydrogen Evolution Reaction." Submitted on September, 2015.

5. Presentations

ACS 250th National Meeting, Boston MA 2015

Thermally stable, crystalline, mixed phase (anatase/rutile) mesoporous titanium dioxide as excellent catalyst for photocatalytic organic pollutants degradation